NASA CONTRACTOR REPORT

NASA CR-1836

A STUDY OF THE STRUCTURE OF JET TURBULENCE PRODUCING JET NOISE

by D. C. Wooten, C. E. Wooldridge, A. J. Amaro, and G. R. Plapp

Prepared by
STANFORD RESEARCH INSTITUTE
Menlo Park, Calif. 94025
for

NATIONAL AERONAUTICS AND SPACE ADMINISTRATION • WASHINGTON, D. C. • JULY 1971

1. Report No.	2. Government Accession No.	3. Recipient's Catalog No.
NASA CR-1836		

4. Title and Subtitle	5. Report Date
A STUDY OF THE STRUCTURE OF JET TURBULENCE PRODUCING JET NOISE	July 1971
	6. Performing Organization Code

7. Author(s)	8. Performing Organization Report No.
D. C. Wooten, C. E. Wooldridge, A. J. Amaro, G. R. Plapp	
	10. Work Unit No.

9. Performing Organization Name and Address	11. Contract or Grant No.
Stanford Research Institute Menlo Park, California 94025	NASW-1938
	13. Type of Report and Period Covered
12. Sponsoring Agency Name and Address	Contractor Report
National Aeronautics and Space Administration Washington, D C. 20546	14. Sponsoring Agency Code

15. Supplementary Notes

16. Abstract

The turbulent structure in the mixing region for the first few diameters downstream from the outlet of a circular subsonic jet is characterized at three Mach numbers, 0.3, 0.5, and 0.7, at two different levels of core turbulence. The velocity and turbulent intensity profiles closely correspond to those measured by other workers. A digital data reduction program was used to calculate auto- and cross-correlations of axial velocity fluctuations ~~and~~ and the power spectral densities. Convection velocities were measured using the overall hot wire signals and using signals that were digitally filtered for band-passes about center frequencies of 0.875, 3.5, and 8.5 kHz. The convection velocities of the lower frequency components of the signals were lower and varied more slowly with radial position than the convection velocities of the higher frequency components and of the overall signal. Thus the large eddies which correspond to the low frequency components are convected at roughly a constant velocity across the shear layer which is about 0.6 of the jet velocity. This corresponds to the convection speed of coherent pressure fluctuations that have been observed across the jet core. This observation supports the hypothesis that the coherent pressure field is driven by the intermittent fluctuations at the core boundary which in turn are related to the large (low frequency) eddies.

17. Key Words (Suggested by Author(s))	18. Distribution Statement
	Unclassified - Unlimited

19. Security Classif. (of this report)	20. Security Classif. (of this page)	21. No. of Pages	22. Price*
Unclassified	Unclassified	83	$3.00

*For sale by the National Technical Information Service, Springfield, Virginia 22151

PREFACE

This study of the structure of turbulence in the noise-producing region of a round subsonic jet was performed principally by the authors. Thanks are due to Dr. R. C. Singleton for writing the computer program used to carry out the digital analysis, and to Mr. Bruce Craig for helping with the analog-to-digital conversion of the hot-wire data.

This project was under the management of Mr. Ira R. Schwartz, Chief, Fluid Mechanics Branch, NASA Headquarters, Washington, D.C.

CONTENTS

CONTENTS (Concluded)

LIST OF ILLUSTRATIONS

ILLUSTRATIONS (Continued)

ILLUSTRATIONS (Concluded)

TABLES

NOMENCLATURE

A,B	Coefficients of hot-wire characteristic (Eq. 1).
a	Speed of sound in air.
a, a_1	Coefficients of change in thermal conductivity of gas with temperature.
D	Jet diameter.
E	Hot-wire voltage.
e	Fluctuating component of hot-wire voltage.
$F(T), g(T)$	Functions of temperature (Eq.9).
f	Frequency.
I	Hot-wire current, turbulent intensity.
i	Fluctuating component of hot-wire current.
$\tilde{K}_1$	Dimensionless wave number.
L_{x1}	Axial length scale of turbulence.
M	Jet Mach number.
N	Number of digital samples per channel.
P_0	Stagnation pressure.
P_1	Barometric pressure.
Q	Ordinate intercept (Eq. 11).
R	Ideal gas constant.
R_{11}	Cross-correlation of axial velocity fluctuations of hot wires separated in axial direction.
R_w	Resistance of hot wire at wire temperature.
r_w	Fluctuating component of R_w.
R_g	Resistance of hot wire at gas temperature.
T_w	Temperature of hot wire.
T_g	Temperature of gas.

t_g	Fluctuating component of T_g.
t	Dimensional time delay.
$\tilde{t}$	Dimensionless time delay.
U	Axial velocity component.
U_o	Jet velocity.
u	Fluctuating component of axial velocity.
u'	RMS axial velocity.
X	Axial coordinate measured from jet exit.
Y	Radial coordinate measured from jet centerline.

Greek Symbols

γ	Ratio of specific heats of air.
Δ	Width of shear layer adjacent to core.
Δx	Axial spacing between hot wire.
η	$= (Y-D/2)/X$

I INTRODUCTION

With the phenomenal growth of air transportation over the last two decades, the contribution of aircraft to the overall noise pollution problem has generated increasing public concern. The greater frequency of takeoffs and landings, the increase in size of transport aircraft, and the expansion of airport facilities have served to increase the noise in many residential communities to a level considered by some to be unacceptable. Current projections of the future growth of air transportation, including the introduction of the supersonic transport (SST) and the flight of V/STOL aircraft into metropolitan and residential areas, give the concern about aircraft noise an immediate priority.

National and international public concern was reflected in the "Transportation Message of 1966" by the President of the United States,[1] the International Symposium on Aircraft Noise held in 1966 in England,[2] which attracted top policy makers from many nations, and the many recent review articles in scientific journals considering possible methods of reducing aircraft noise.[3-8] Therefore, aircraft noise has become a major consideration in the design of aircraft engines, the expansion and layout of airport facilities, and the takeoff and landing procedures required by most major airports.[9]

It is generally agreed that for the large subsonic jet transports of the early 1970s, the jet noise has been largely reduced by means of large, cold-air bypass ratios ranging from 5:1 to 8:1, by the use of multiple nozzles, and by nozzle shaping to induce external air flow.[2,6,7] For

these engines the major part of the noise is created by the air inlet compressor, although current research indicates that this problem can be alleviated.* In fact, through the use of acoustic treatment, the compressor noise in the engines used in the jumbo jets has been greatly reduced. Utilizing these developments together with higher climb angles (6° instead of the present 3°), the current engine generation is giving rise to lower perceived noise levels, between 19 and 20 db lower (10 db $\sim$ 1 order of magnitude) than those of the previous generation of jets, such as the older fan jets (707/DC8) which operate with a bypass ratio of only 3:2.

This reduction in perceived noise level, however, is largely offset by heavier planes with larger engines and by increased air traffic. The present improvements therefore represent only a temporary engineering solution. Further improvements will require technical break-throughs that must be founded upon a fundamental understanding of the noise production processes.

For the SST with subsonic combustion, the problem of jet noise is even more severe, although in this case too, some improvement can be made by means of steeper climb angles, bypass doors in the afterburner, etc. However, the severe profile drag in supersonic flight does not permit the construction of large bypass fans. Also, the dependence of shock compression on correct alignment of the engine air inlet makes the SST engine more susceptible to stall, and therefore it is much more difficult to utilize noise suppression schemes in the design of such engines.

Except for the sonic boom produced by the SST, noise from both subsonic and supersonic aircraft originates primarily from the propulsion

---

* "Noise Abatement Method and Apparatus," U.S. Patent No. 3194487.

system; i.e., the propeller, the helicopter rotor, or the jet engine.[10] In the jet engine the compressor, the combustion chamber, and the exhaust jet all contribute to the overall noise level. In general, the combustion noise is much less than that due to the other two sources. In the jet engines currently used on all but the new jumbo jets, the jet exhaust is the dominating noise contributor. By using a high bypass ratio in the new engine design for the jumbo jets, however, the jet exhaust noise has been reduced so that the compressor noise becomes the primary noise source. By acoustic treatment of the engine nacelle, however, progress has been made in reducing the compressor noise to more acceptable levels,[4] again leaving the exhaust jet as the main contributor to the noise problem in the subsonic jet engines. For the SST, in which large, cold-air bypass ratios cannot be achieved easily and afterburning is necessary, the jet noise will probably always be the dominant noise source. The research program described herein addresses, therefore, the exhaust jet noise problem. Hopefully, study of the fundamental processes of noise generation will bring new technological breakthroughs to alleviate the noise problem associated with the continuing growth of the air transportation field.

Over the past two decades, the problem of aircraft noise has been studied both theoretically and experimentally. The theoretical groundwork was done primarily by Lighthill[7,11-13] in England before the mid-1950s. Although Lighthill is still active in the field,[7] relatively recent advances in the jet noise theory have been contributed by Powell,[14,15] Williams,[16,17] and others. Experimentally, relatively few investigators have addressed themselves to actual experimental research on the details of the jet exhaust mixing process that gives rise to the sound field.[18-20] Except for Davies, Fisher, and Barratt,[20] who made hot wire correlation measurements inside the jet, most investigators satisfied themselves with varying gross parameters such as jet diameter,[10,21] velocity,[22-24] density,[24] etc., while measuring the spectral content, direction, and

magnitude of the radiated sound. From these investigations an overall picture of exhaust jet noise generation has emerged, which is in good qualitative agreement with observed noise levels and directivity. However, it will be necessary to study experimentally the basic jet structure in more detail to gain a better understanding of the noise generation process.

The research program described in this report seeks a better understanding of the turbulence structure in the noise-producing region of a round jet. Measurements of turbulence intensities, spectra, and mean velocity profiles were made with a hot-wire anemometer in a 1-1/2-in. diameter jet at ambient temperature and with ambient external conditions. These measurements were made at axial positions corresponding to 2, 4, and 8 outlet diameters from the exit, at jet Mach numbers of 0.3, 0.5, and 0.7, and with two different initial levels of turbulence in the core. To induce the higher level of core turbulence, a screen was placed in the jet nozzle just upstream of the exit. Time-delay correlations between the axial velocity fluctuations measured at points separated longitudinally were carried out with the upstream wire located at the axial position stated above. The signals were correlated in several frequency bands as well as over the complete signal band. These measurements were used to calculate the convection speed and general decay characteristics of different eddy sizes. The results of these experiments are to be used to interpret known characteristics of noise outside the jet as measured by other investigators and to gain a better theoretical understanding of the noise production mechanisms.

II INSTRUMENTATION

Jet Apparatus

The test setup used is shown schematically in Fig. 1. It is essentially a blow-down system and consists simply of a settling chamber and two 500-gal, 200-psi air supply tanks. The settling chamber is 60 in. long and 8 in. in diameter and is fitted with a 1-1/2-in. alluminum nozzle. The full length of the chamber was taken up by an installation of screens and fiber glass that was designed to isolate the nozzle from valve and feeder-line disturbances, both acoustic and aerodynamic. The screens consisted of a series ranging from coarse to fine mesh (4 to 100). A 1-in. layer of fiber glass was installed around the inside periphery of the settling chamber.

Hot Wire Apparatus and Related Instrumentation

Measurements of mean velocity and turbulent intensity profiles were made using a constant temperature hot-wire aneomometer system manufactured by Thermo-Systems Inc. A block diagram of the total anemometer instrumentation is shown in Fig. 2. The hot-wire probes consisted of 0.2-mil diameter tungsten wire, 3/32 in. long, mounted on needle tips. The needles, 1/2 in. long, were secured by a 5-1/4 X 1/4-in. heavy wall stainless steel tube. The probe units were attached to a vibration-dampened mount connected to a heavy steel frame having micrometer screwslides for two-dimensional positioning (see Fig. 3). The probe signals were fed into the anemometer 5:1 bridge at an overheat ratio of 1.5. The bridge output for the mean voltage was then filtered through a direct galvanometer equipped

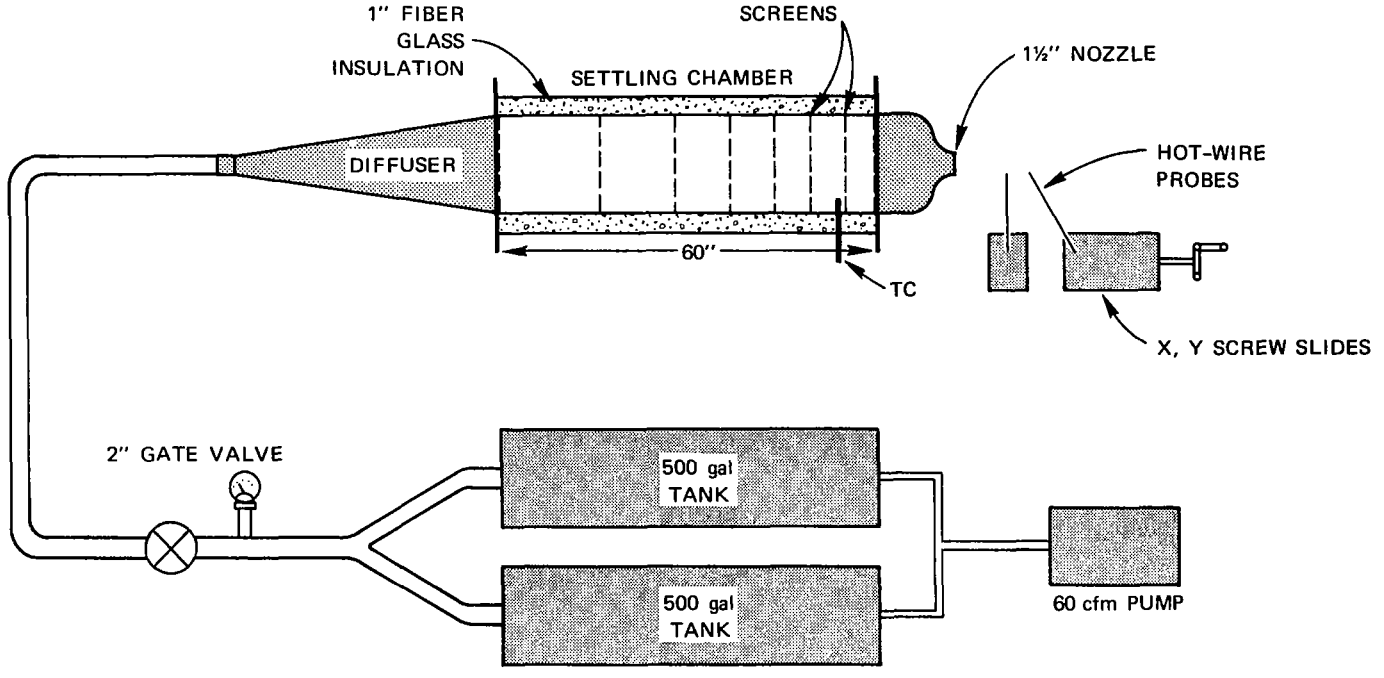

FIGURE 1 SCHEMATIC DIAGRAM OF JET NOISE TEST SYSTEM

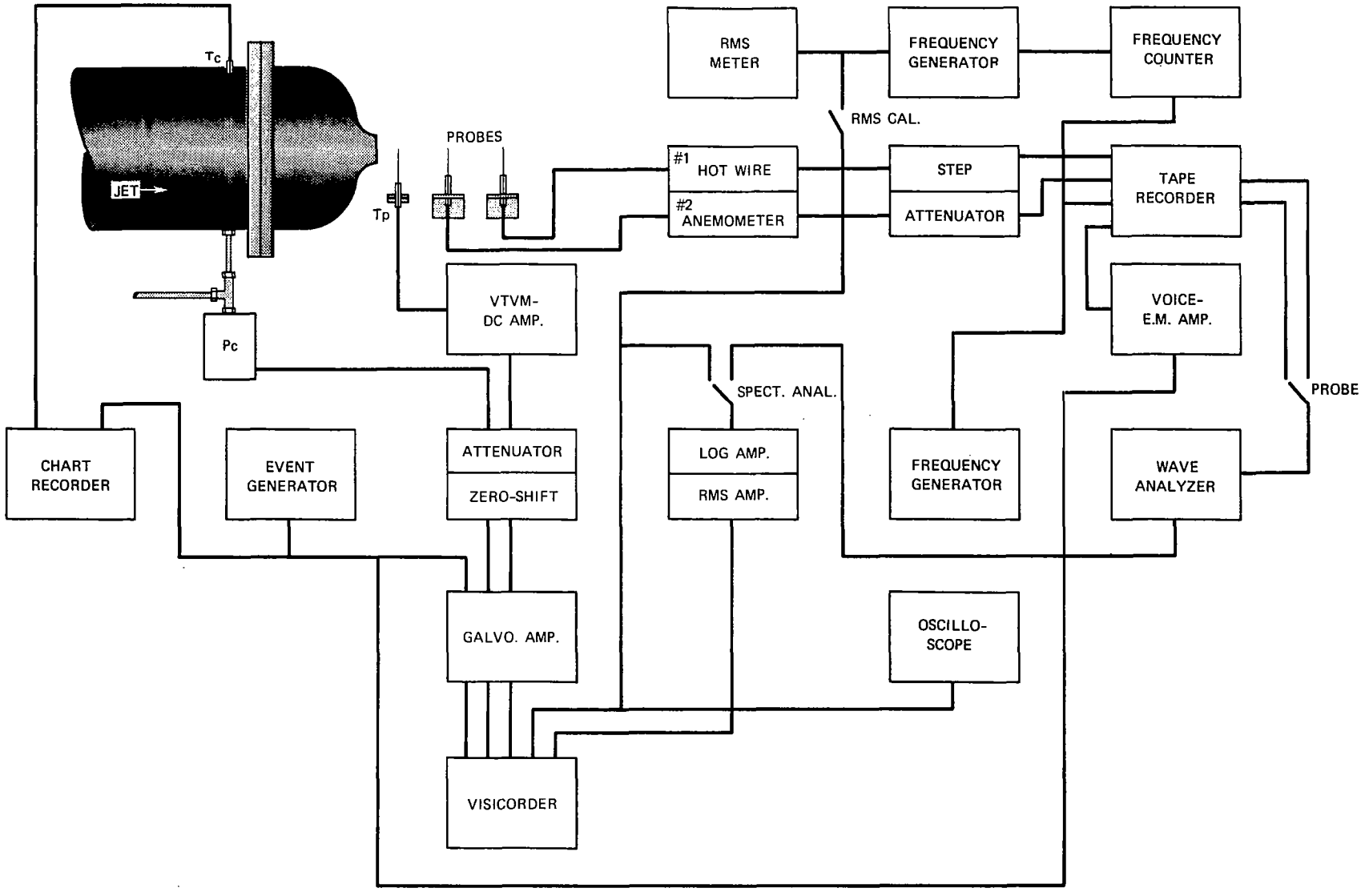

FIGURE 2 SCHEMATIC DIAGRAM OF INSTRUMENTATION

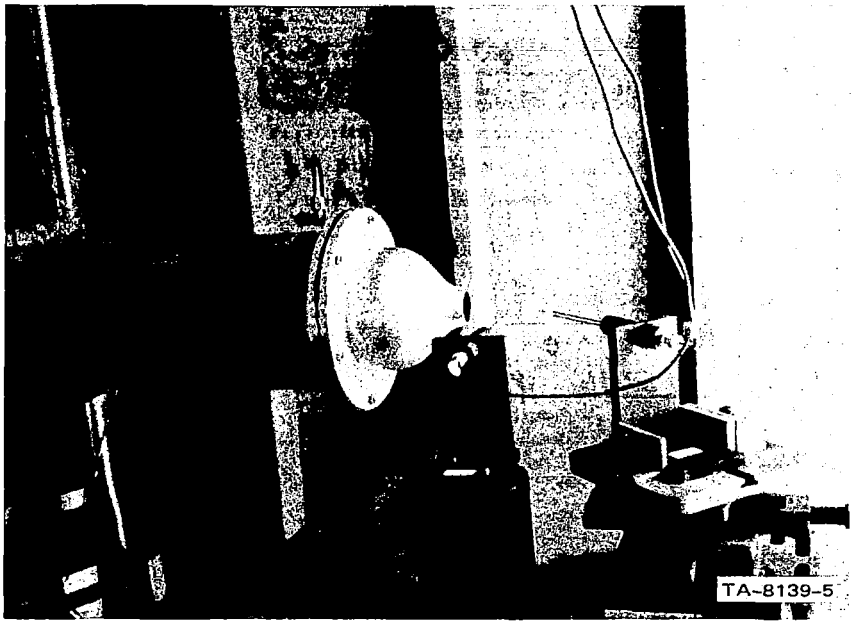

FIGURE 3 HOT-WIRE PROBE ASSEMBLY

with a visicorder. For the fluctuating voltage component, a signal conditioner was incorporated. The signal conditioner provided gains of 1, 10, or 100 with a band-pass filter of 5 Hz to 50 kHz. The output of the conditioner was fed into a two-stage operational amplifier consisting of a logarithmic amplifier and an rms meter amplifier having a time constant of 1 sec. The resultant signal was then recorded on the visicorder. The signals are 0.1% accurate with a frequency response of approximately 100 kHz and an inherent noise level of 0.02% in a 10-Hz bandwidth. In principle, a constant temperature anemometer instantaneously measures fluid flow parameters by sensing the heat transfer rate (heat flux) between an electrically heated sensor and the flow medium. The basic signal depends on the fluid composition, mass flow, and temperature difference. For many measurements density is constant and the instrument measures velocity. When the jet temperature varies, compensation in the mean

operating conditions is required, otherwise a 6% error results for each $20^{\circ}C$ change in temperature.

Hot-wire sensitivity

Because of the necessity of using a blow-down system to provide the mass flow for the jet, the jet temperature is lower than that of the surroundings, and both velocity and temperature fluctuations are present in the mixing region of the jet. Constant-current operation of a hot wire will lead to sensitivity to both fluctuation modes, whereas constant-temperature operation is sensitive only to velocity fluctuations. This behavior can be demonstrated by following the arguments of Hinze.[25]

The basic equation describing hot-wire response is

$$\frac{I^2 R_w}{R_w - R_g} = A + B\sqrt{U} \tag{1}$$

For a linear relationship between thermal conductivity and temperature, the factor A is given by [25]

$$A = \frac{A_g}{a + a_1 T_g}\left[a + \frac{a_1}{2}(T_w - T_g)\right] + \frac{a_1 A_g}{a + a_1 T_g} T_g \tag{2}$$

Expanding Eq. (1) and using Eq. (2) gives an equation for the fluctuating wire resistance in the constant-current case or the fluctuating current in the constant-temperature case. In the former case, Hinze[25] obtains

$$\frac{I^2 r_w}{\bar{R}_w - \bar{R}_g} = \left[\frac{\bar{A} + B\sqrt{\bar{U}}}{\bar{R}_w - \bar{R}_g} + \frac{A_g a_1}{2b(a + a_1 T_g)R_g}\right] r_w$$

$$+ \left[\frac{A_g a_1}{2(a + a_1 T_g)} - \frac{\bar{A} + B\sqrt{\bar{U}}}{\bar{R}_w - \bar{R}_g} CR_0\right] t_g$$

$$+ B\sqrt{\bar{U}}\,\frac{u}{2\bar{U}} \qquad (3)$$

where r_w, t_g, and u are the fluctuations of R_w, T_g, and U.

A similar expression can be obtained in the constant-temperature case, although Hinze does not give a derivation for it. The result is

$$\frac{2\bar{I}R_w}{R_w - \bar{R}_g}\, i = \frac{A_0 a_1}{2(a + a_1 T_0)}\, t_g + B\sqrt{\bar{U}}\,\frac{u}{2\bar{U}} \qquad (4)$$

Comparing the temperature fluctuation sensitivity terms in Eqs. (3) and (4), one can see a common term and an additional term in the constant-current case. As Hinze [25] points out, the substitution of reasonable numerical values for the quantities involved shows that the common coefficient is negligible in comparison to the other terms. Thus, the constant-temperature approach is perfect for the measurement of velocity fluctuations, which is desired in the present case, but it cannot be used for the measurement of temperature fluctuations.

Data Handling and Hot-Wire Calibration

Velocity calibration and temperature compensation were carried out in the following manner. The method allows for changes in fluid

temperature without the use of a temperature-compensated probe, (which is usually of slow response).

The hot-wire voltage E and the jet temperature T are recorded on magnetic tape or on a visicorder at a constant-nozzle Mach number for an extended run. The Mach number is determined by a simultaneous pitot tube measurement, making use of the following derived equation

$$M = \sqrt{\frac{2}{\gamma - 1}\left(\left(\frac{P_o}{P_1}\right)^{\frac{\gamma - 1}{\gamma}} - 1\right)} \qquad (5)$$

P_o = absolute stagnation press

P_1 = barometric pressure

γ = specific heat ratio of air

The temperature decreases as a result of emptying the tank. Corresponding values of E and T were read at the same time instant and plotted in the form E vs. T. This procedure was followed for each constant-nozzle Mach number M so that lines could be drawn through the points of constant Mach number as shown in Fig. 4. Vertical constant-temperature lines were then drawn on the curve. Values of E were taken from the intersections of the constant T and constant M lines. These values are plotted as log E vs. log M for constant T as shown in Fig. 5. This plot is a power function of the following form:

$$\log E = \log E_o + B \log M \qquad (6)$$

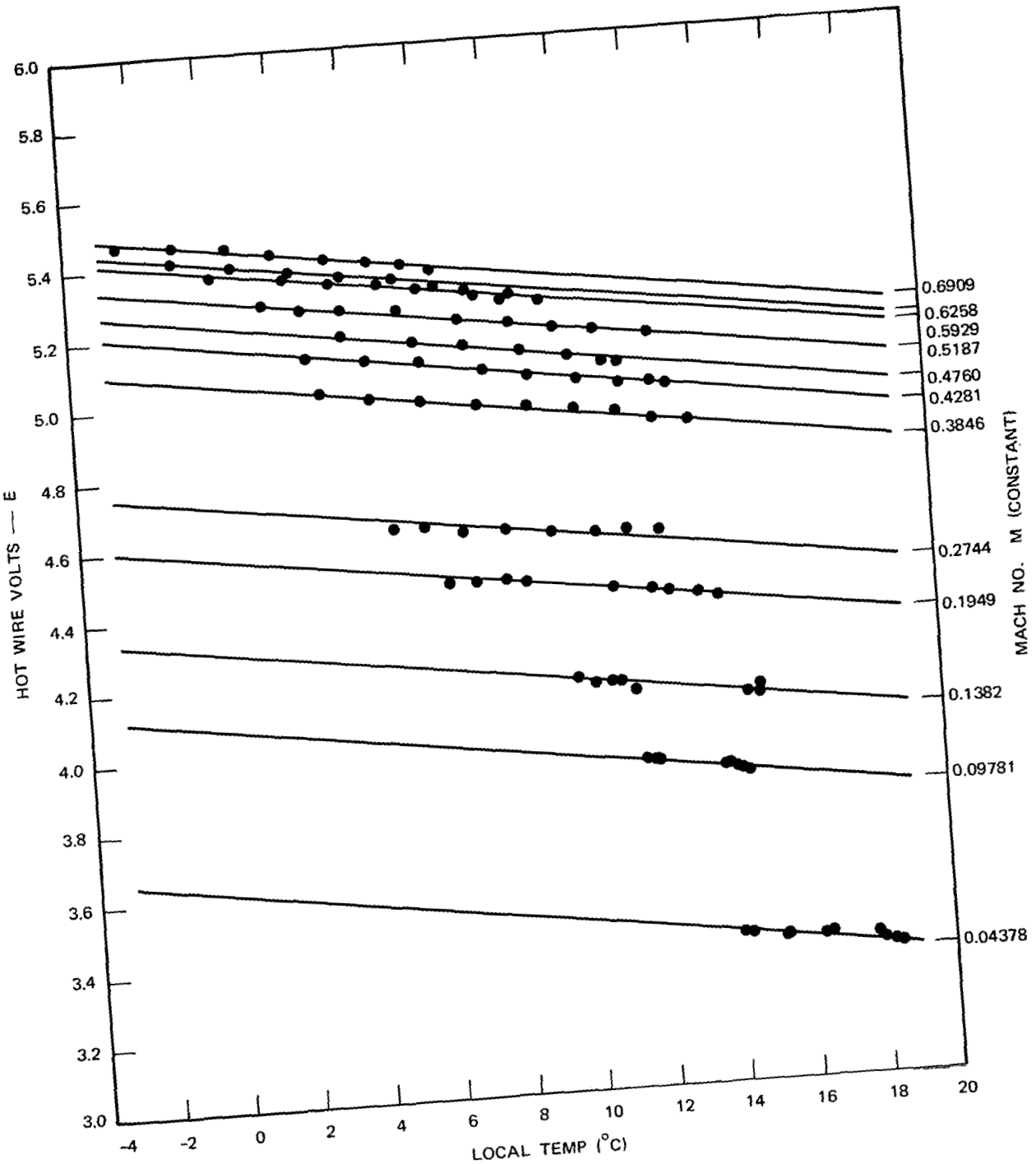

FIGURE 4 HOT-WIRE VOLTAGE VERSUS LOCAL JET TEMPERATURE

or

$$E = E_o M^B \tag{7}$$

where E_o is the intercept at M = 1.0 and B is the slope of the line in the log-log plot.

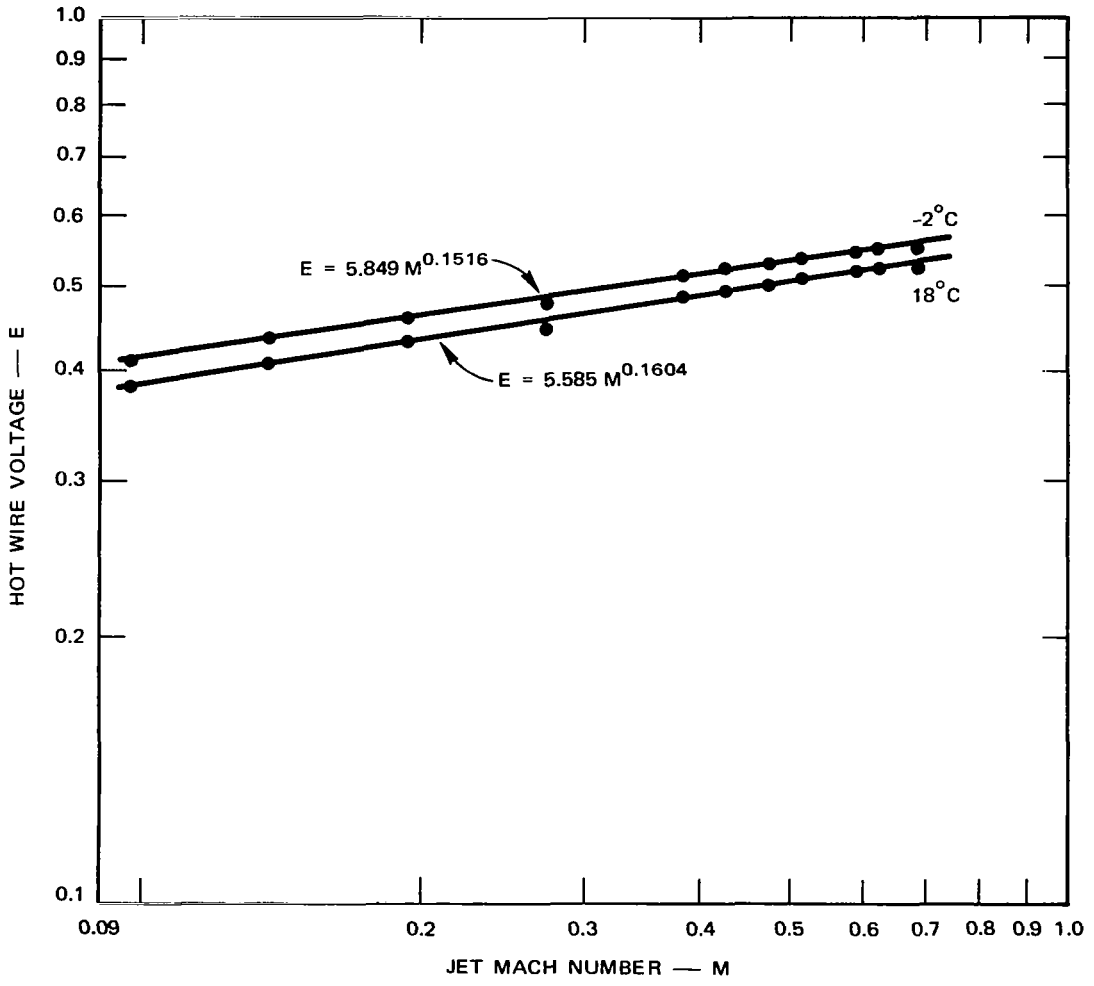

FIGURE 5 HOT-WIRE VOLTAGE VERSUS JET MACH NUMBER

Now solving for M in Eq. (7) we get:

$$M = \left(\frac{E}{E_o}\right)^{\frac{1}{B}} \tag{8}$$

where $B = f(T)$ and $E_0 = g(T)$.

The functions f(T) and g(T) were found by the best curve fit for plots of B vs. T and E_0 vs. T, respectively. Substituting these relationships into Eq. (8) gives the following:

$$M = \left(\frac{E}{g(T)}\right)^{\frac{1}{g(T)}} \tag{9}$$

But the Mach number is also

$$M = \frac{u}{a} \tag{10}$$

where u is the local velocity and a is the local velocity of sound at temperature T. Solving Eq. (10) for the local velocity u gives

$$u = Ma \tag{11}$$

The velocity of sound is given by

$$a = \sqrt{g_o \gamma RT} \tag{12}$$

For air $\gamma = 1.4$, $R = 53.3 \frac{ft - lb}{lmb - {}^{o}R}$, and $g_o = 32.2 \frac{lb_m - ft}{lb - sec}$

For T in ^{o}K

$$a = 65.75\sqrt{T(^{o}K)} \tag{13}$$

Now substituting Eqs. (9) and (13) into Eq. (11) we finally arrive at the relationships described in the following:

The local jet velocity is:

$$u = 65.75\sqrt{T(^{\circ}K)}\left[\frac{E}{g(T)}\right]^{\frac{1}{f(T)}} \tag{14}$$

To calculate the local turbulent intensity, the following formula is used

$$\frac{\sqrt{\overline{u^2}}}{U} = \frac{4}{1 - \frac{Q^2}{E^2}} \frac{\sqrt{\overline{e^2}}}{E} \tag{15}$$

where values for $\sqrt{\overline{e^2}}$ and E are taken simultaneously for local conditions at a local fluid temperature.

Q is the ordinate intercept at M = 0 (or very small M) on an E vs. M plot. For very small M, Eq. (7) is now:

$$Q = E_o M^B\big|_{M<<<1} \tag{16}$$

so, by substitution of B = f(T) and E_o = g(T) into Eq. (6), we get:

$$Q = g(T)M^{f(T)}\big|_{M<<<1} \tag{17}$$

This value is now used in Eq. (15) to give turbulent intensity.

The Eqs. (16) and (17) with the appropriate empirical variables were incorporated into a small Tymshare computer program, Fig. 6. The data input consists of the local jet temperature T, the probe mean voltage E, and the associated rms value R of the fluctuating component. Figure 7 illustrates a typical Tymshare output.

Three types of turbulence data were obtained: turbulent intensities, space correlations, and frequency spectra. In all cases, these were

```
5 PRINT "JET NØISE PRØJECT #8319"
10 DIM V(40),I(40),M(40),A(40),T(40),Y(40)
20 READ X,M,Z,D,S,Y1
30 PRINT "TEST NØ.";S
35 LET X1 = X/1.5
40 PRINT "AXIAL DIST. FRØM NØZZLE X/D=";X1
50 PRINT "MACH NØ. AT NØZZLE =";M
60 IF Z = 10 THEN 70
65 PRINT "HIGH NØZZLE TURBULANCE"
66 GØ TØ 80
70 PRINT "LØW NØZZLE TURBULANCE"
80  PRINT "Y/D","V/VMAX","I*V/VMAX","VEL.(FT/SEC)","TURB.INT."
85 LET YO = 1.5E-10
90 FØR K = 1TØD
100 READ E,T1,R
105 LET T = T1+273.18
106 LET P =(2.832E-2)+(4.54804E-4)*T
107 LET T(K)=T
110 LET B =1/P
120 LET EO =9.39849-(1.30916E-2)*T
130 LET V(K) = 65.75*(SQR(T))*(E/EO)↑B
131 LET M(K)=(E/EO)↑B
133 LET A(K)=V(K)/M(K)
135 LET Q =EO*(1E-03)↑P
140 LET I(K) = (4/(1-(Q↑2/E↑2)))*(R/E)
150 LET Y = YO/1.5
155 LET YO = YO+Y1
156 LET Y(K)=Y
160 LET V1 = V(K)/V(1)
170 LET L = I(K)*V1
180 PRINT Y,V1,L,V(K),I(K)
190 NEXT K
200 PRINT "Y/D","MACH","VEL.SØUND","TEMP.DEG.K"
210 FØR J =1TØD
220 PRINT Y(J),M(J),A(J),T(J)
230 NEXT J
235 END
```

FIGURE 6 TYMSHARE COMPUTER PROGRAM

JET NØISE PRØJECT #8319
TEST NØ. 116
AXIAL DIST. FRØM NØZZLE X/D= 2
MACH NØ. AT NØZZLE = .685
LØW NØZZLE TURBULANCE

Y/D	V/VMAX	I*V/VMAX	VEL.(FT/SEC)	TURB.INT.
1.00000E-10	1	1.99451E-02	777.028	1.99451E-02
6.66667E-02	.998269	2.42427E-02	775.683	2.42847E-02
.133333	.987933	3.68781E-02	767.652	3.73285E-02
.2	.994497	6.37602E-02	772.753	.064113
.266667	.995902	6.72001E-02	773.844	6.74766E-02
.333333	.995902	8.27078E-02	773.844	8.30481E-02
.4	.932533	.106522	724.605	.114229
.466667	.768227	.100659	596.934	.131027
.533333	.534671	8.47596E-02	415.455	.158527
.6	.322618	.071792	250.683	.222529
.666667	.145268	4.72599E-02	112.877	.32533
.733333	5.78805E-02	2.03579E-02	44.9748	.351724
.8	3.66185E-02	9.72934E-03	28.4536	.265694
.866667	2.67849E-02	6.29783E-03	20.8126	.235127
.933333	2.41781E-02	4.13224E-03	18.787	.170908
1.	2.14236E-02	3.46011E-03	16.6467	.161509

Y/D	MACH	VEL.SØUND	TEMP.DEG.K
1.00000E-10	.69126	1124.08	292.28
6.66667E-02	.690182	1123.88	292.18
.133333	.683738	1122.73	291.58
.2	.688635	1122.15	291.28
.266667	.69032	1120.99	290.68
.333333	.69032	1120.99	290.68
.4	.645286	1122.92	291.68
.466667	.530954	1124.27	292.38
.533333	.369344	1124.84	292.68
.6	.222367	1127.34	293.98
.666667	9.98555E-02	1130.4	295.58
.733333	3.96793E-02	1133.46	297.18
.8	2.50528E-02	1135.74	298.38
.866667	1.83251E-02	1135.74	298.38
.933333	1.65361E-02	1136.13	298.58
1.	.014662	1135.36	298.18

FIGURE 7 TYPICAL TYMSHARE DATA OUTPUT

limited to the axial component of the turbulent velocity. In addition to these data, there were the usual aerodynamic measurements necessary to determine flow velocities, density, temperature, and barometric pressure.

Figure 8 indicates the flow regions investigated in the present tests. Flow from a jet can be divided into the three regions denoted in the figure by A, B, and C. Region A extends from the nozzle exit to

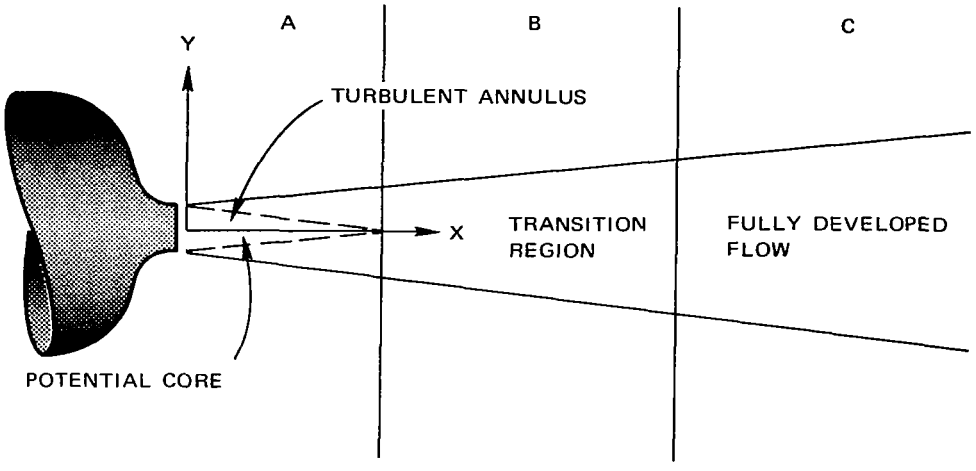

FIGURE 8 JET FLOW REGIONS

5 to 6 diameters downstream of the nozzle and contains the potential core, or unmixed fluid, and a surrounding turbulent annulus, which is characterized by high turbulence levels and large shear forces. In region B, which extends from the potential core to about 10 to 15 diameters from the nozzle, the entire cross section is characterized by intense turbulence. However, the flow is not yet fully developed in region B; this state occurs at points downstream of this transition region, i.e., in region C.

The tests discussed herein were limited to regions A and B, since these regions are of greatest significance in noise generation by a turbulent jet.

Analog-to-Digital (A-D) Conversion of Fluctuating Data

A block diagram of the instrumentation used for the A-D conversion is illustrated in Fig. 9. The anemometer analog data signals were tape recorded at 60 inches per second (dc to 20 kHz range) and were played back on the same machine (all data were recorded using the same recording lead), Precision Instruments Model 207, at a 4:1 speed reduction of 15 inches

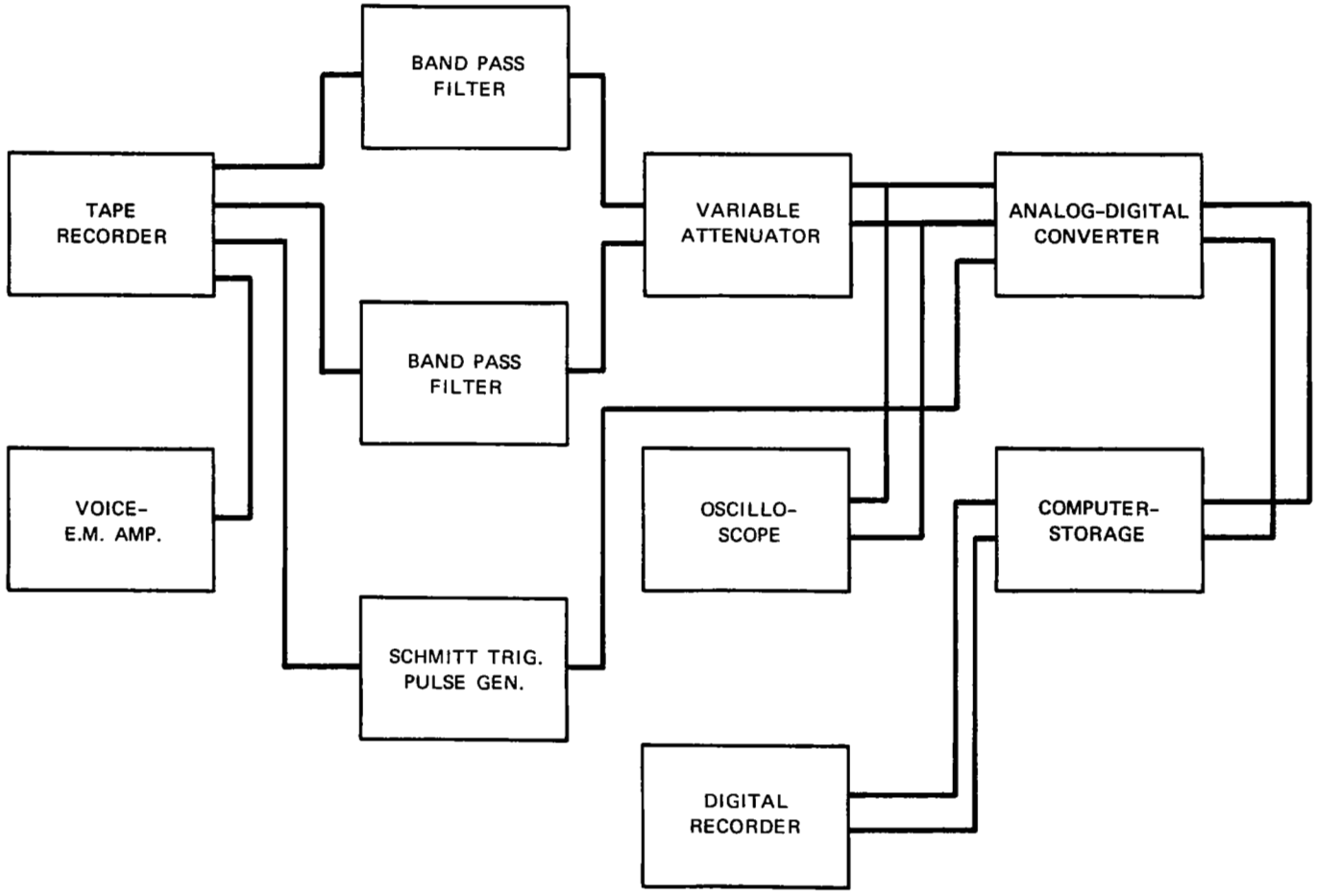

FIGURE 9 ANALOG-DIGITAL INSTRUMENTATION

per second (dc to 5 kHz range). This rate was necessary in order to be within the sampling rate limitations of the Scientific Data Systems (SDS) 12-channel (multiplexed) A-D converter and to be within the storage-handling capabilities of the SDS 930 computer. The two tape recorder outputs corresponding to hot-wire probes A and B were each fed into a Krohnhite model 310-ABR 24-db/octave band-pass filter passing 5 Hz to 5 kHz to eliminate any dc signal and prevent any possible fold-over of higher frequencies in the conversion. The filtered signals were then fed through a dual precision attenuator, before being sent into the converter, to adjust for optimum signal levels without the occurrence of any limiting. The A-D converter, for all practical purposes (i.e., to within 25 μsec) sampled each signal simultaneously using a high-speed multiplexed sampling rate of 10 kHz at 2 samples per 5-kHz frequency limit. The sampling rate was determined by the 10-kHz timing signals from the tape by use of a Schmitt trigger pulse generator which in turn drove the converter unit. This method compensated for any tape speed variations and allowed a very accurate spectral analysis of the data.

The SDS 930 computer was programmed for the A-D conversion to take 2048 samples per computer record. Each record consisted of 1024 samples from each probe channel. Ten sec of data (2-1/2 sec real time data because of the 4:1 tape speed reduction) was usually taken per jet noise test which comprised 100 computer records. The A-D conversion program called for continuous storage using alternating buffers, which allowed continuous recording of digital data on tape at a bit density of 800 per inch. The no-gapping-on-tape between records allowed very accurate time correlation studies of all frequencies. The digitized data were then ready to be run through the comprehensive time correlation and spectrum analysis computer program, which is described in the next section of this report.

Digital Data Analysis

The data analysis computations were performed on a CDC 6400 computer, using a spectral analysis program developed by Singleton and Poulter[26] for single-channel data, but extended to two-channel data.

Data segments of duration 102.4 msec (4096 sample values/channel) were used in the analysis. The data were read into the computer, and the two input signals were then plotted as a visual check on the A-D conversion process. All plots were made on line, using a CDC 280 microfilm plotter. The data on each channel were then multiplied by the data window function

$$\sin^2(\pi j/N) \qquad \text{for } j = 0,1,\ldots N-1 \ .$$

to reduce interaction of spectral estimates.

The windowed data were then transformed to the frequency domain, using a fast Fourier transform subroutine, and the auto- and cross-spectra computed. These results were then transformed back to the time domain to yield the auto- and cross-correlation functions. For the autocorrelation functions, the lags corresponding to the first zero crossings were interpolated and listed on the plots. For the cross-correlation functions, a search was made for the largest peak, and the (three-point) interpolated value and corresponding lag were listed in the plot.

The results were then transformed back to the frequency domain, and an additional step introduced to reduce core storage requirements for intermediate results. The auto- and cross-spectra were scaled for unity power in each channel, then smoothed to gain statistical stability--once with three-point triangular smoothing, then twice with 15-point triangular smoothing. The corresponding correlation window is

$$\cos^2(\pi j/N)\left[\frac{\sin(8\pi j/N)}{8\ \sin(\pi j/N)}\right]^4$$

The results for the two channels were then plotted using a log-log scale (db vs. octave).

III JET CHARACTERIZATION

To determine the effectiveness of the settling chamber and acoustic treatment in suppressing noise from the flow control valves, measurements of the turbulence level (Fig. 10) and the turbulence spectrum (Fig. 11) in the jet at the nozzle exhaust were made.

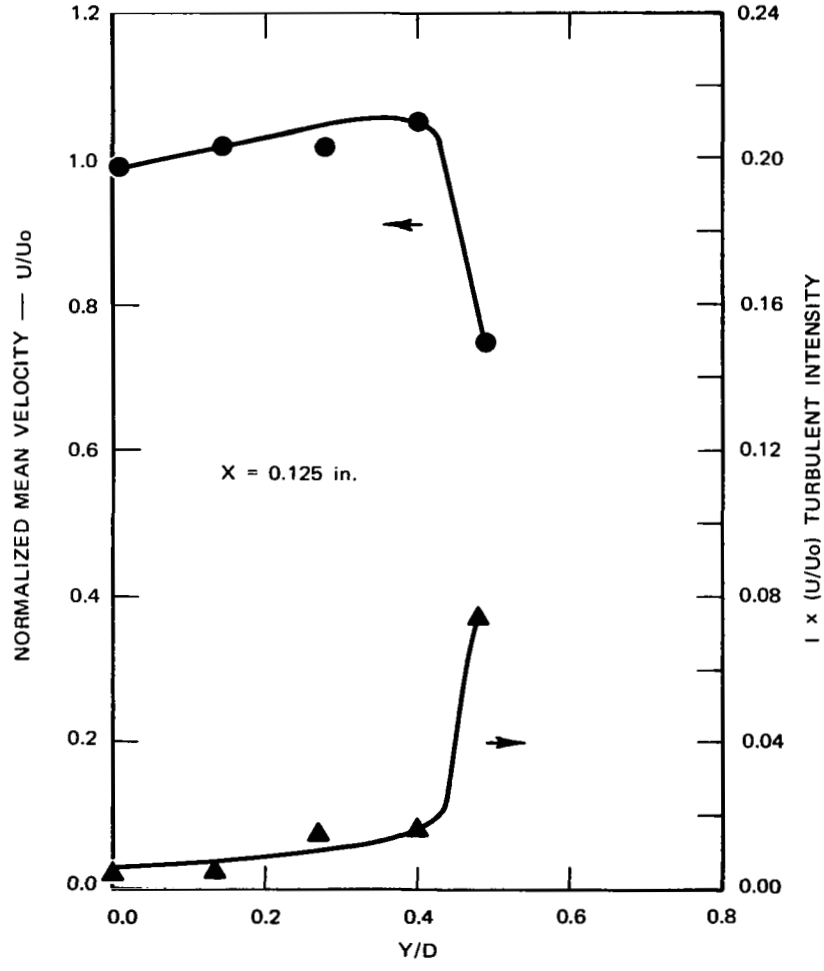

FIGURE 10 MEAN VELOCITY AND TURBULENT INTENSITY VERSUS DISTANCE FROM JET CENTERLINE

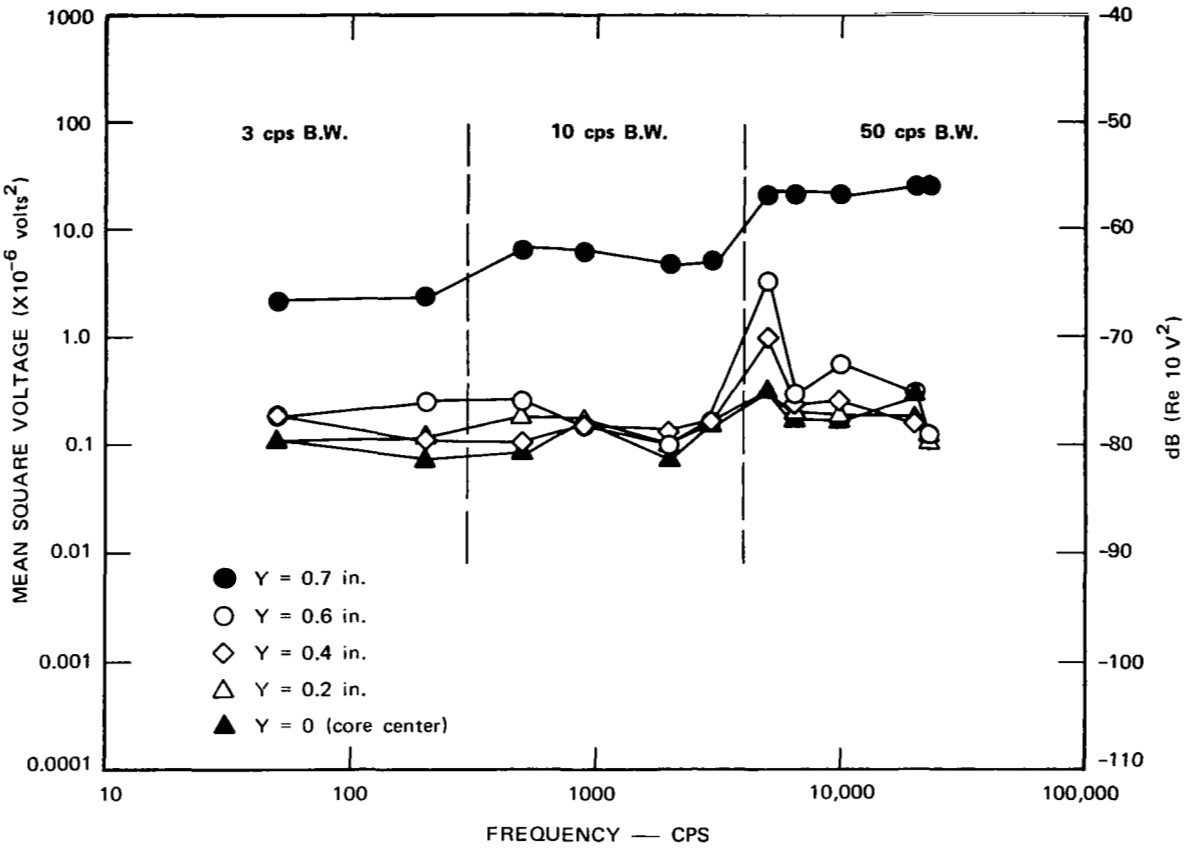

FIGURE 11 SPECTRUM ANALYSIS AT X = 0.125 inch FOR VARIOUS RADIAL POSITIONS

A full characterization of the jet was then undertaken to determine the overall jet characteristics and check for any anomalous flows. Turbulent and mean velocity components were measured across the jet at longitudinal positions corresponding to 2, 4, and 8 outlet diameters from the exit, at jet Mach numbers of 0.3, 0.5, 0.7.

When the turbulent spectrum analysis of the jet was performed, it was evident that several anomalies were present at 6.5, 13, and 23 kHz. Figure 12 shows the effects of an attempt to prevent the main 2-in. flow valve from frosting up as a result of differential pressure drop. Heating tape was used to heat the valve, and the resultant downstream disturbance was evidenced by an increase of the high frequency turbulence component. When the heating was discontinued, the anomalous peaks disappeared. It

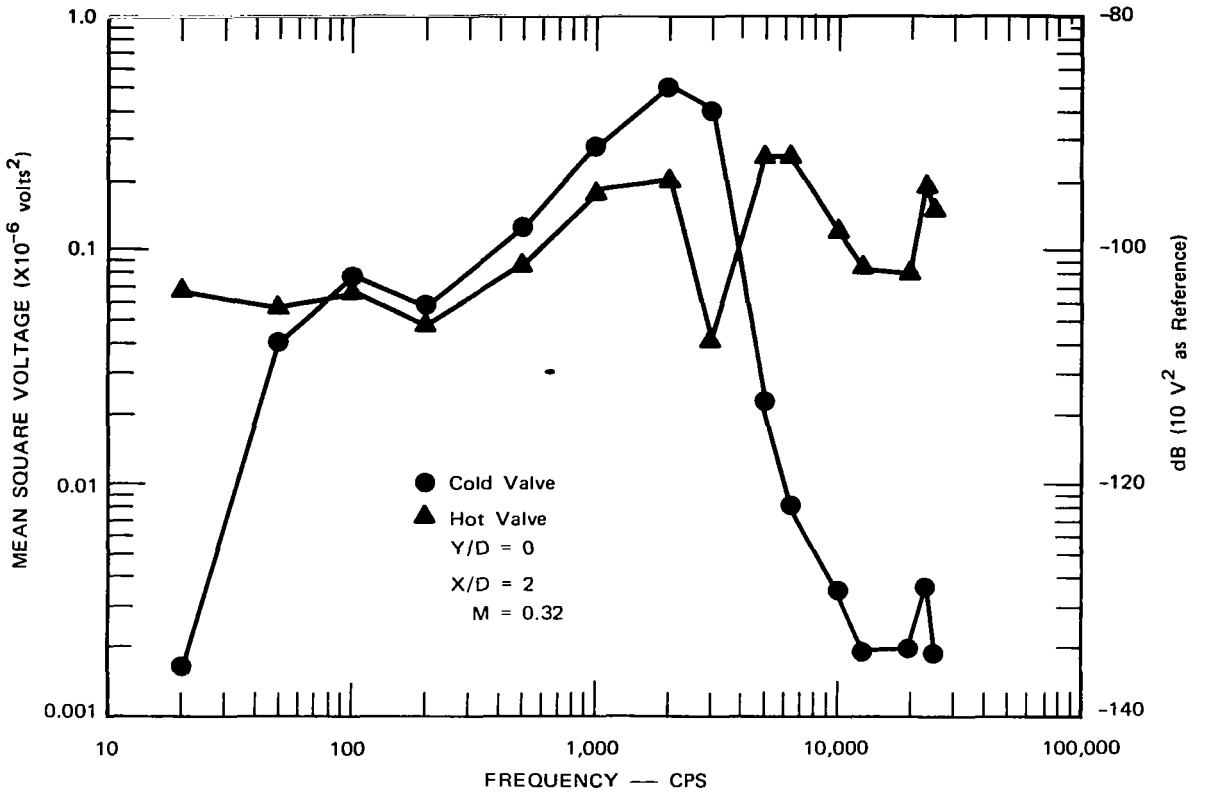

FIGURE 12 COMPARTIVE SPECTRUM ANALYSIS FOR HOT - VERSUS COLD-FLOW VALVE

was also found that high frequency peaks occurred approximately 20 sec into a test (Fig. 13) and that 30 sec was required in order to establish undisturbed flow. Initial turbulent intensity profiles are shown in Figs. 14, 15, and 16. At the high Mach numbers, an excessive amount of turbulence was detected just within the jet core boundary at a Y/D of 0.2, (X/D = 2). Intensive investigation revealed that two factors were involved in producing the anomalies. The first was diffuser stall. The origianl diffuser was used to expand air from a 2-in. supply pipe into a 6-in. setting chamber. A 10° semiangle cone with splitter plates was used for the diffuser. The flow from the diffuser was irregular and measurements at the downstream side of the last screen in the settling chamber just before the entrance to the jet nozzle showed that these

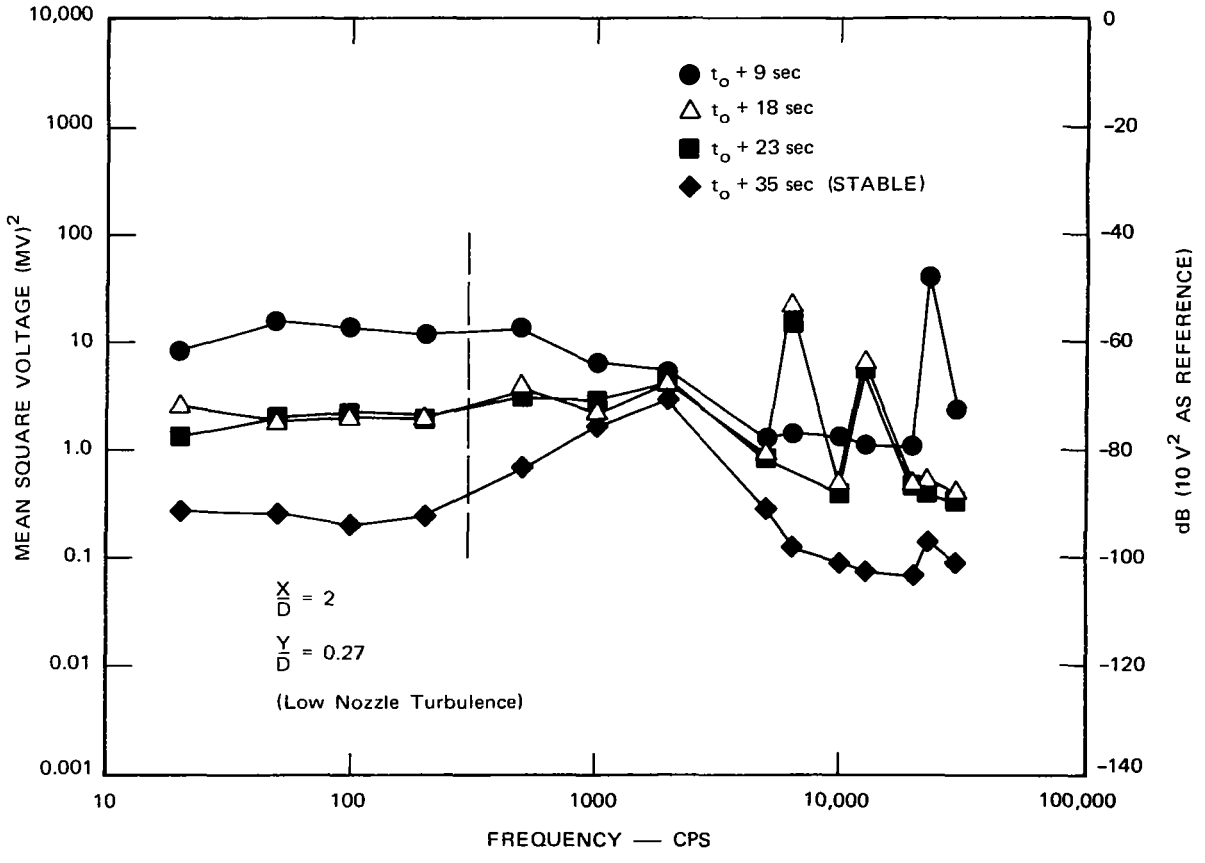

FIGURE 13 JET SPECTRUM AT M = 0.32

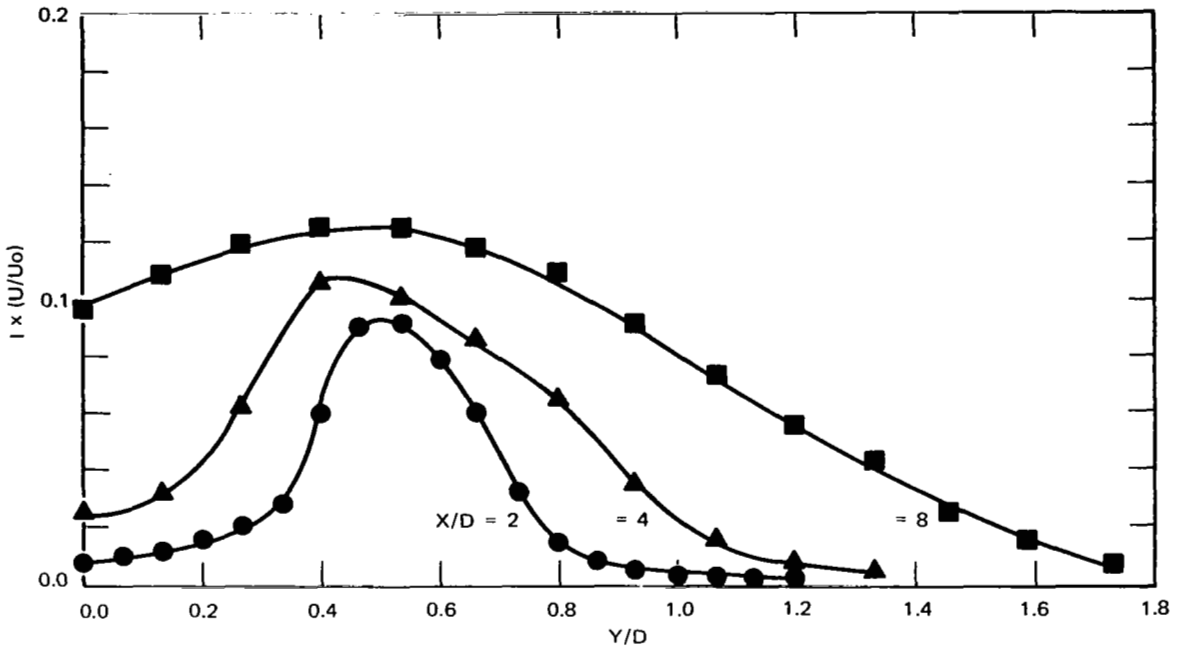

FIGURE 14 TURBULENT INTENSITY AT M = 0.32 FOR VARIOUS X/D

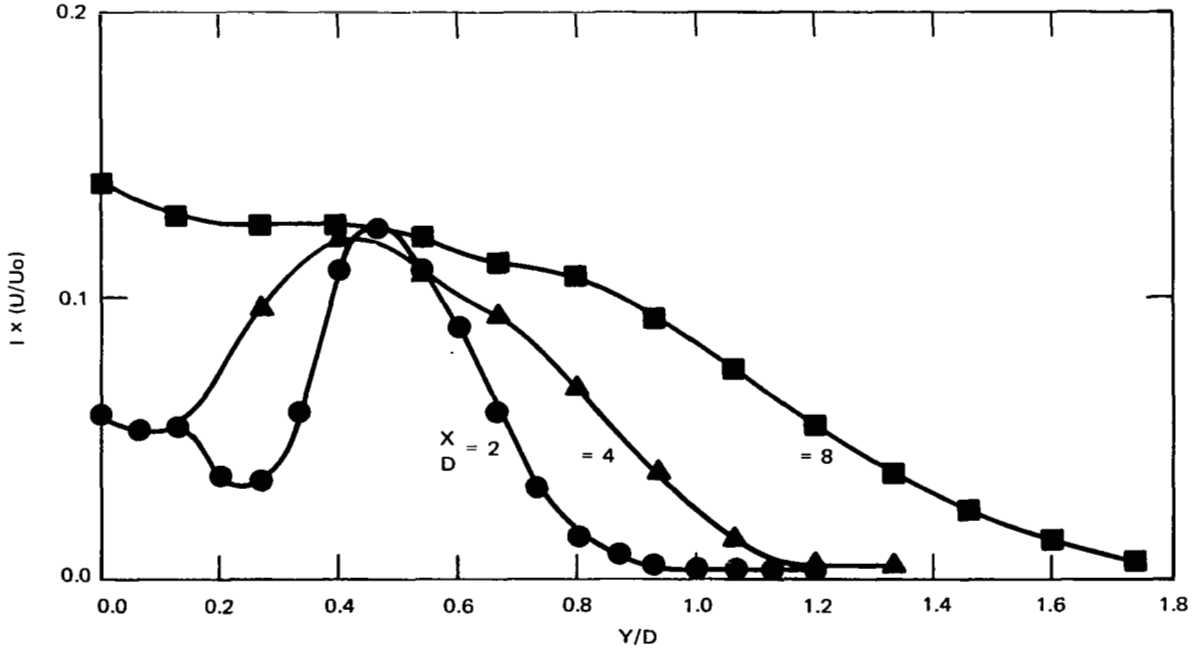

FIGURE 15 TURBULENT INTENSITY AT M = 0.51 FOR VARIOUS X/D

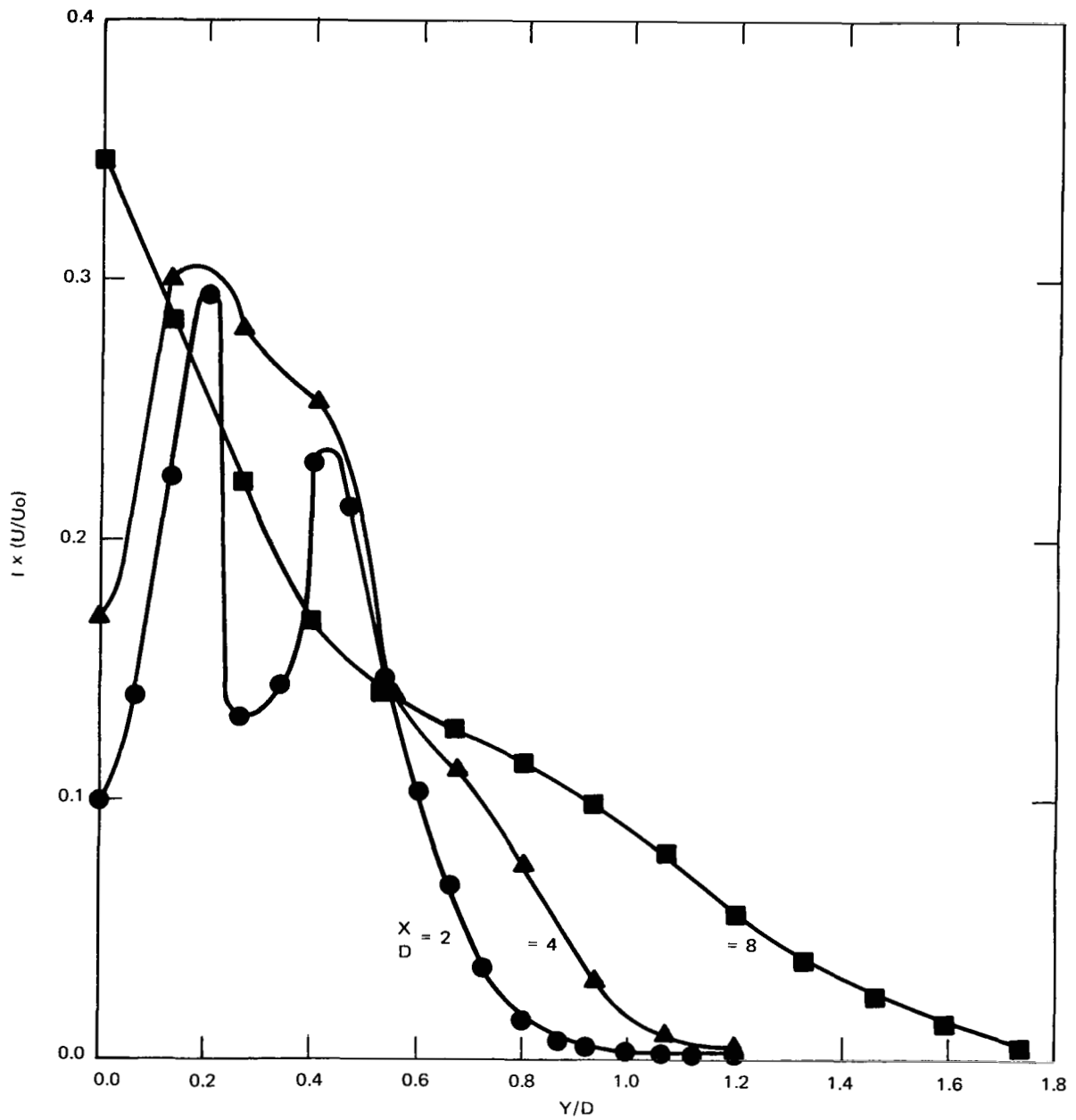

FIGURE 16 TURBULENT INTENSITY AT M = 0.68 FOR VARIOUS X/D

disturbances were not entirely removed by the acoustically treated chamber. Thus, a new diffuser with a 4° half-angle was installed and the results are illustrated in Fig. 17. Notice that even with the 4° diffuser there was evidence of a similar disturbance, although of a lesser magnitude. This disturbance was found to be induced by the thermocouple placed below and slightly downstream of the hot-wire probe. The removal of the thermocouple resulted finally in the anomally-free turbulent intensity profile shown in Fig. 17.

Typical results for the turbulent intensity profile at $X/D = 2$ are shown in Fig. 18. The results obtained at $X/D = 4$ and 8 show a broadening of the peak as X/D increases, corresponding to the broadening of the mixing region and an increase in intensity in the core region as its end is approached. A composite plot of velocity profile and turbulent intensity illustrated in Fig. 18 shows that the maximum turbulent intensity is observed at a radial position that corresponds to the nozzle lip at $Y/D = 0.5$.

Mean Velocity Profiles

Typical results for the mean velocity profile shape are shown in Figs. 19 through 24, where X is the longitudinal coordinate, Y is the lateral coordinate, and D is the diameter of the jet. Three axial positions were studied in each case: one, $X/D = 2$, in the region where the core has a sizable width; one, $X/D = 4$, near the end of the core region; and one, $X/D = 8$, near the fully developed flow region. It can be seen that for all the profiles, $U/U_0 \cong 0.5$ at $Y/D = 0.5$; i.e., on a straight line drawn downstream from the lip of the nozzle. This behavior implies that the mixing region is symmetric as it grows both into the core and into the surrounding ambient air. The velocity profiles for comparison at the various Mach numbers 0.3, 0.5, and 0.7 shown in Fig. 25 indicate fairly uniform exit velocities and show that the decreases in the streamwise direction are about the same in each case. Two different initial

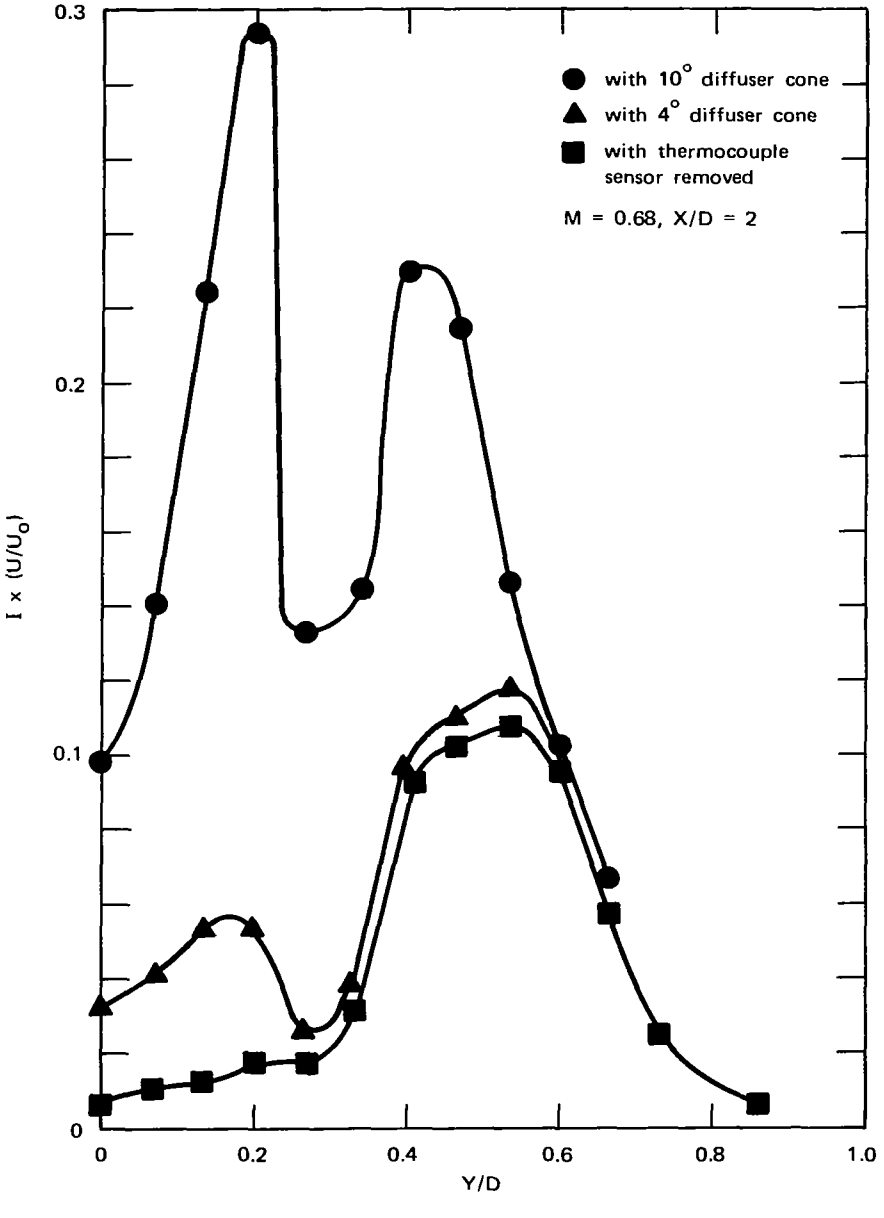

FIGURE 17 COMPARATIVE TURBULENT INTENSITY BEFORE AND AFTER IMPROVEMENTS

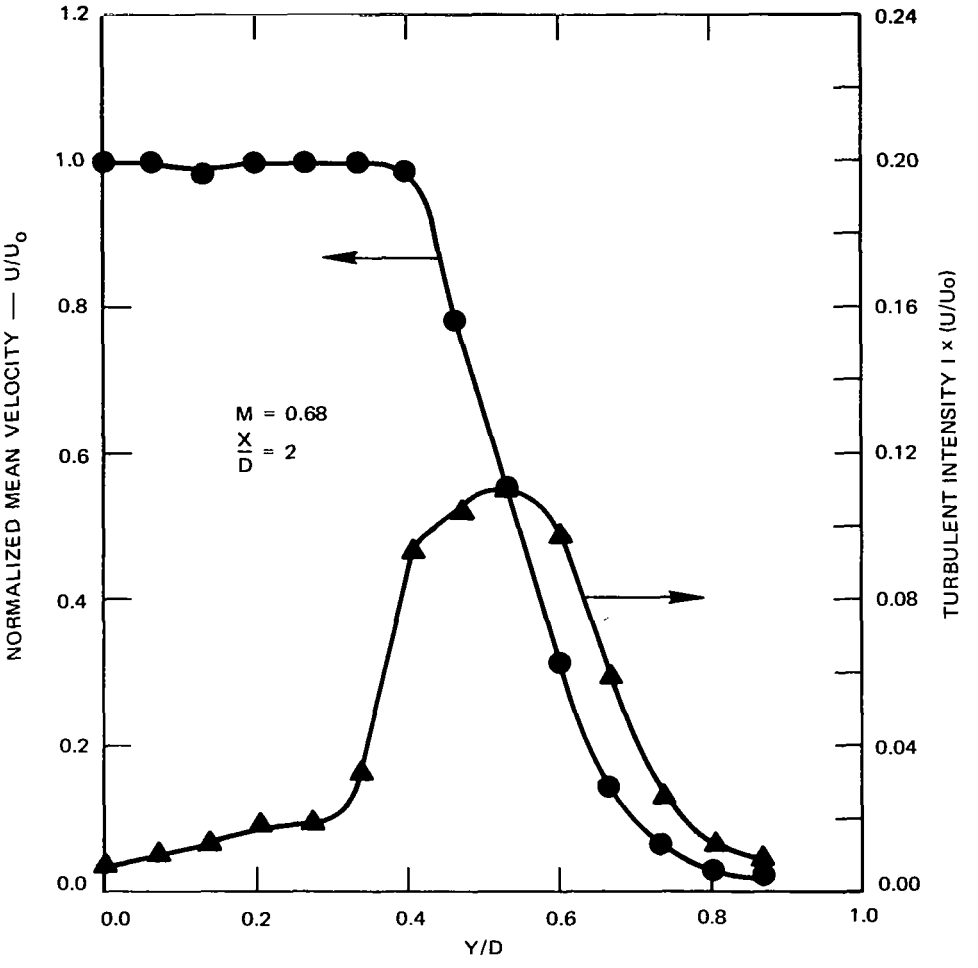

FIGURE 18 COMPOSITE VELOCITY AND TURBULENT INTENSITY PROFILES

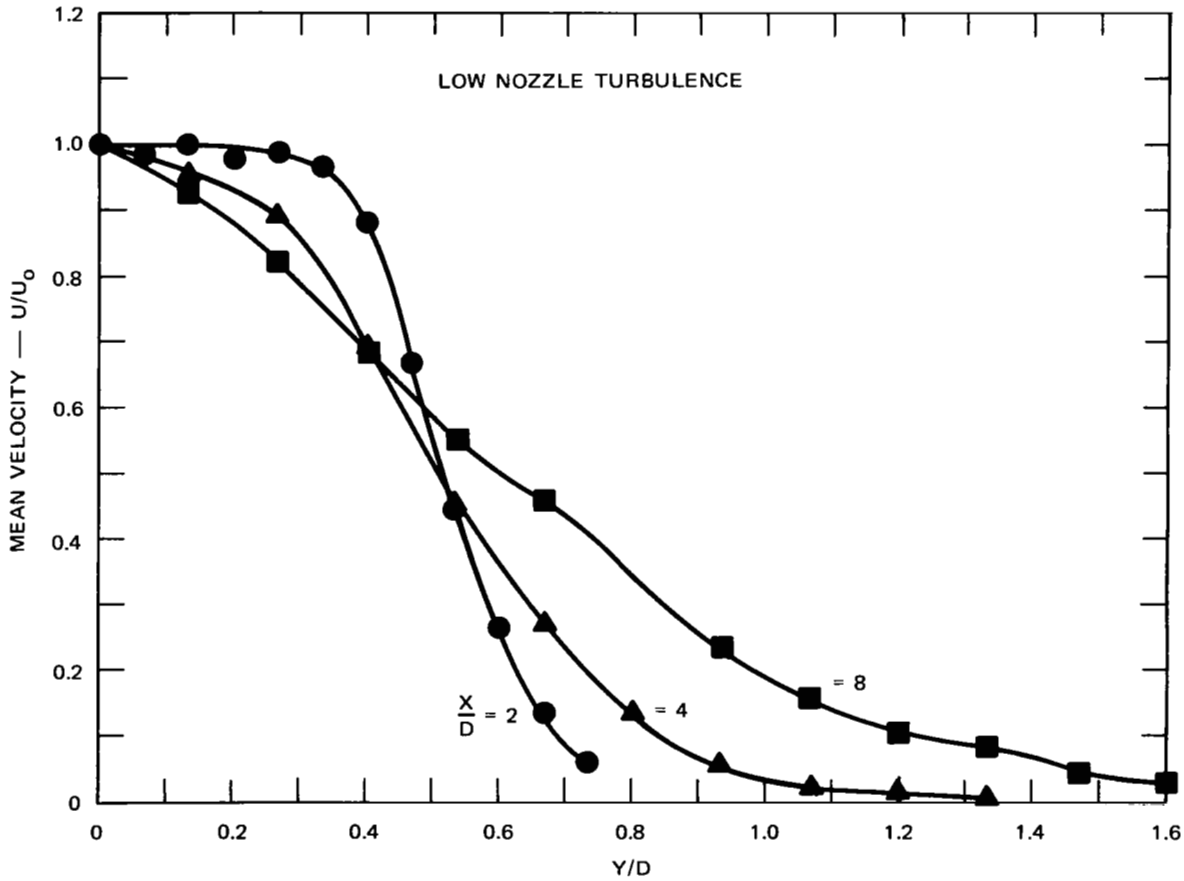

FIGURE 19 JET VELOCITY PROFILES FOR M = 0.32 AT VARIOUS X/D

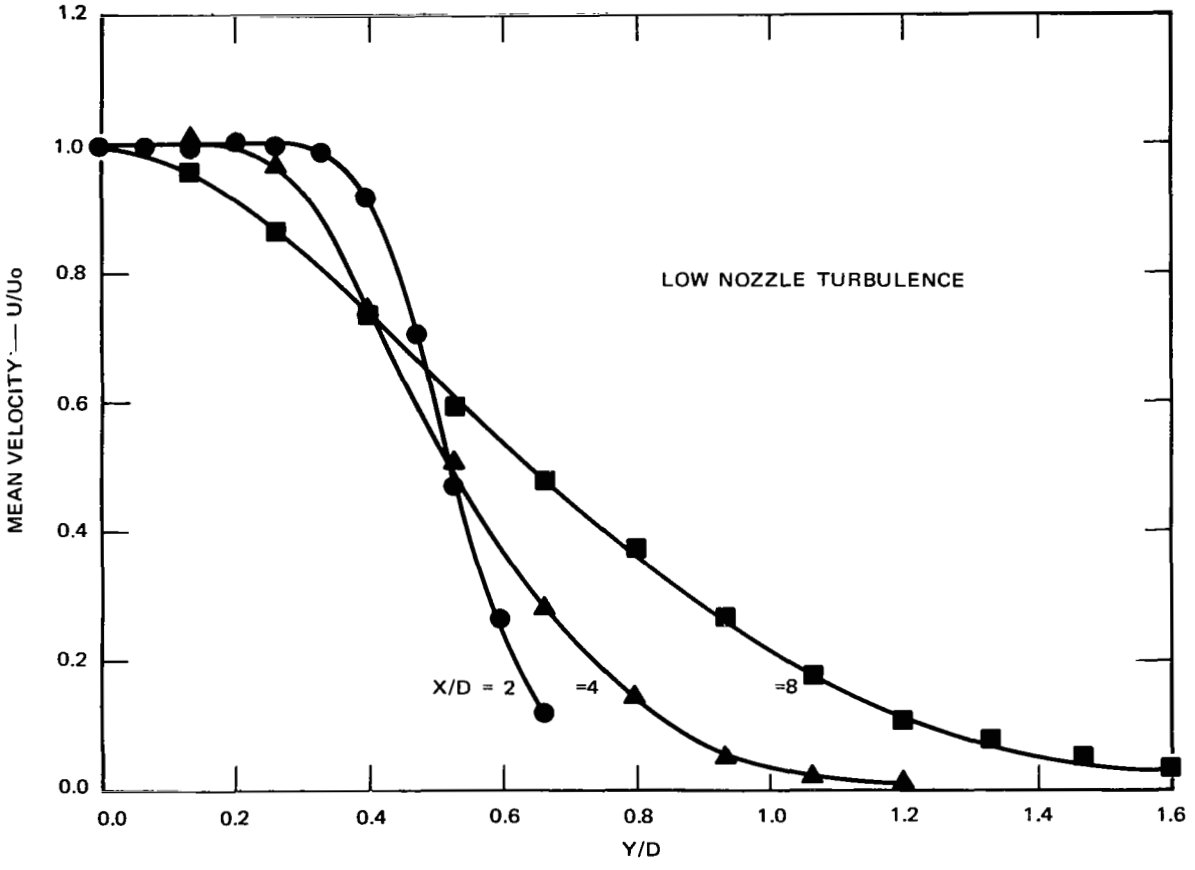

FIGURE 20 JET VELOCITY PROFILES FOR M = 0.51 AT VARIOUS X/D

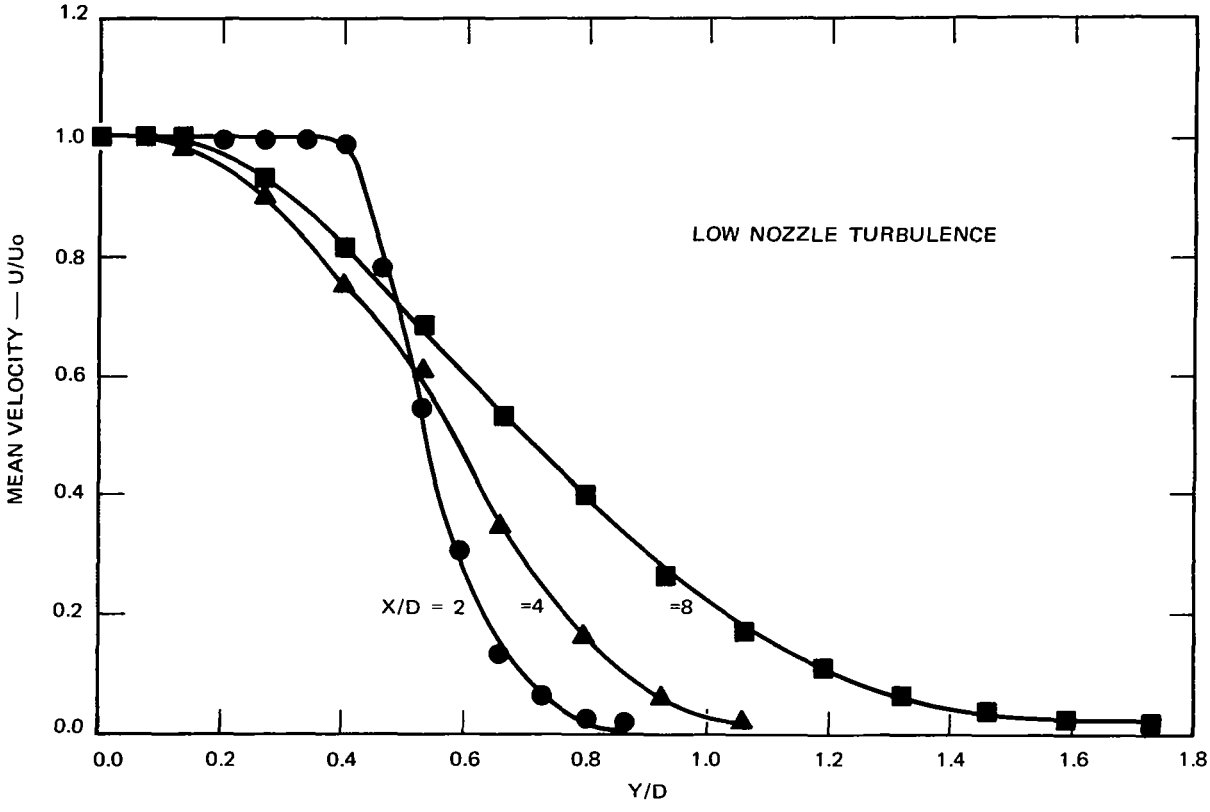

FIGURE 21 JET VELOCITY PROFILES FOR M ≈ 0.68 AT VARIOUS X/D

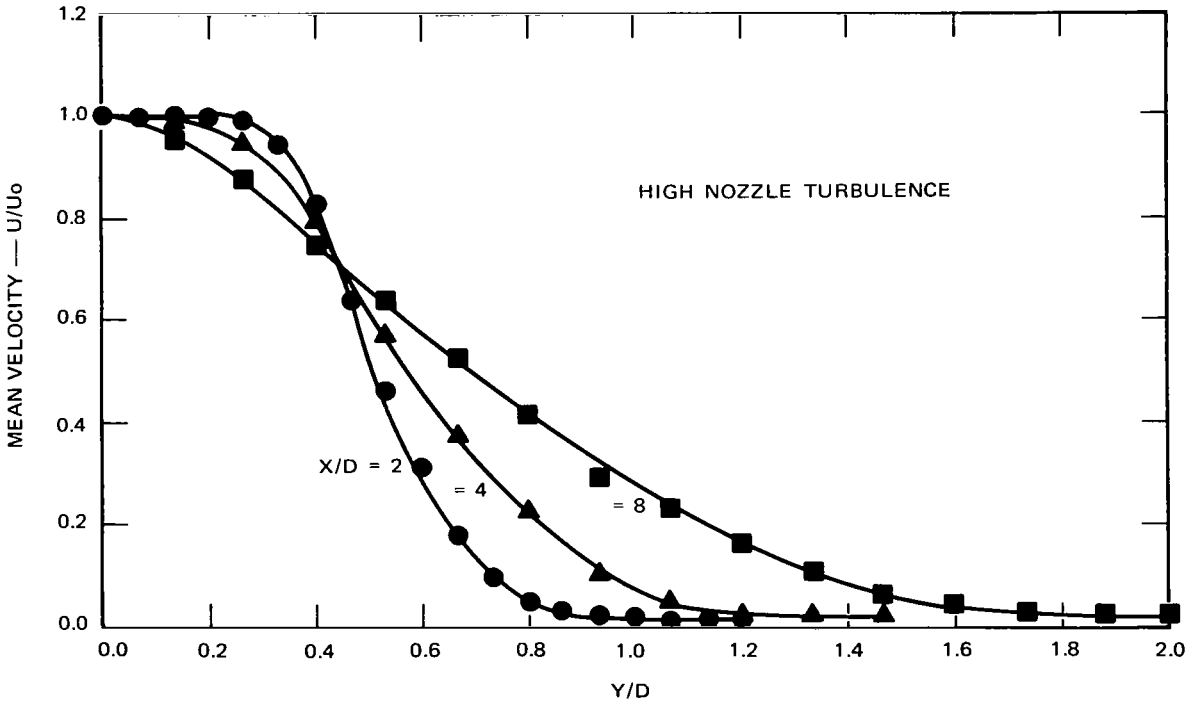

FIGURE 22 JET VELOCITY PROFILES FOR M = 0.32 AT VARIOUS X/D

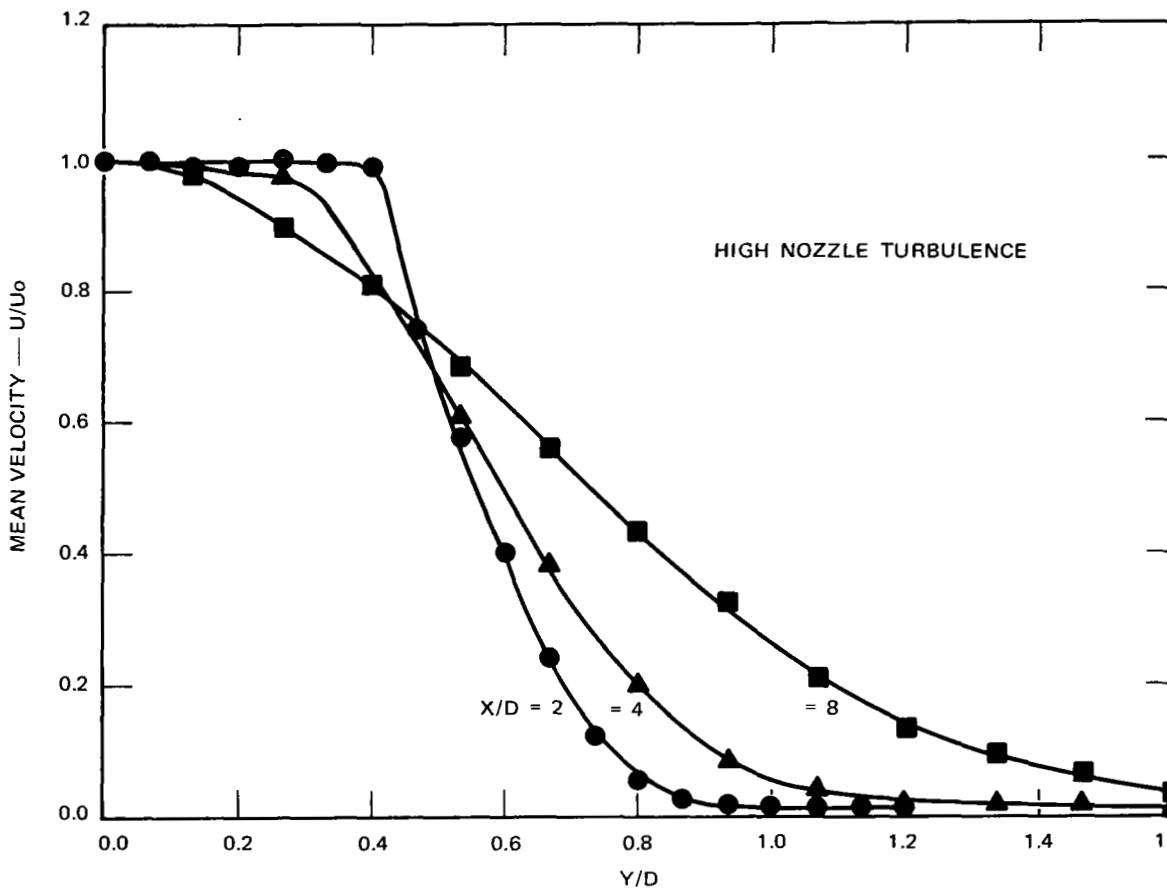

FIGURE 23 JET VELOCITY PROFILES FOR M = 0.51 AT VARIOUS X/D

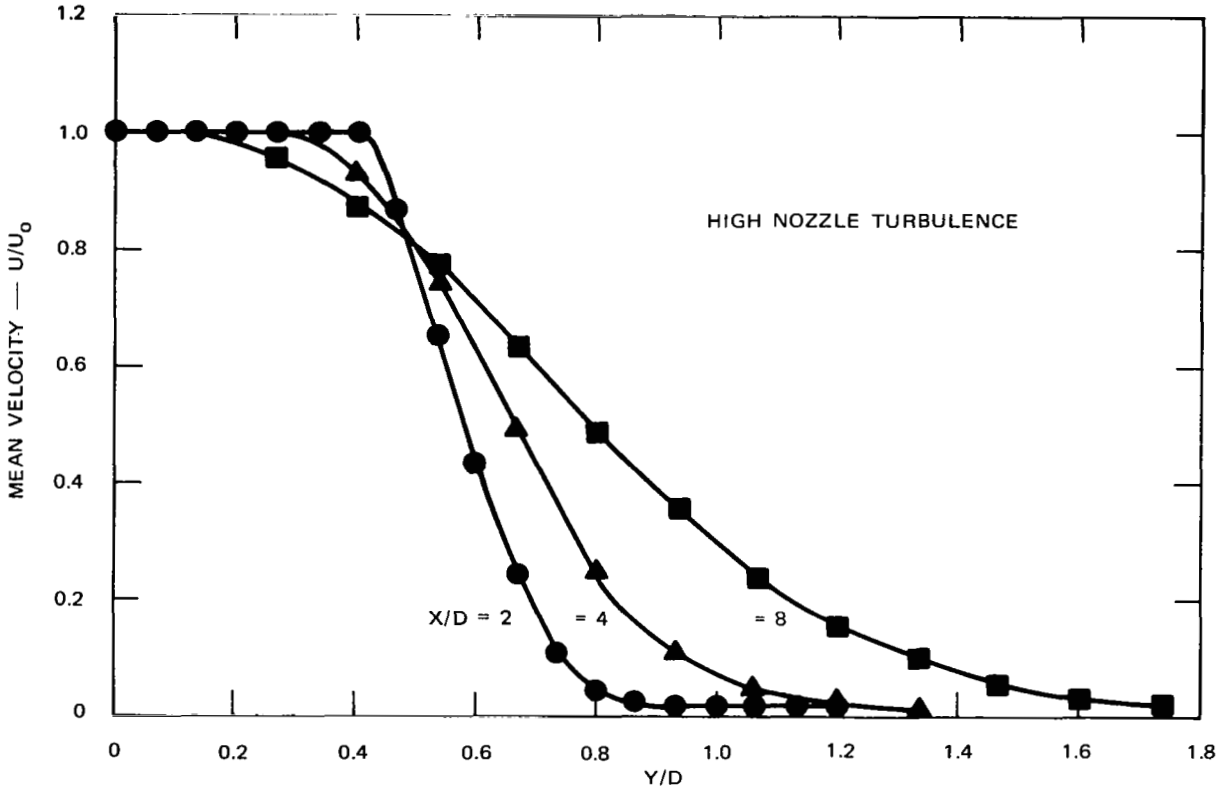

FIGURE 24 JET VELOCITY PROFILES FOR M = 0.68 AT VARIOUS X/D

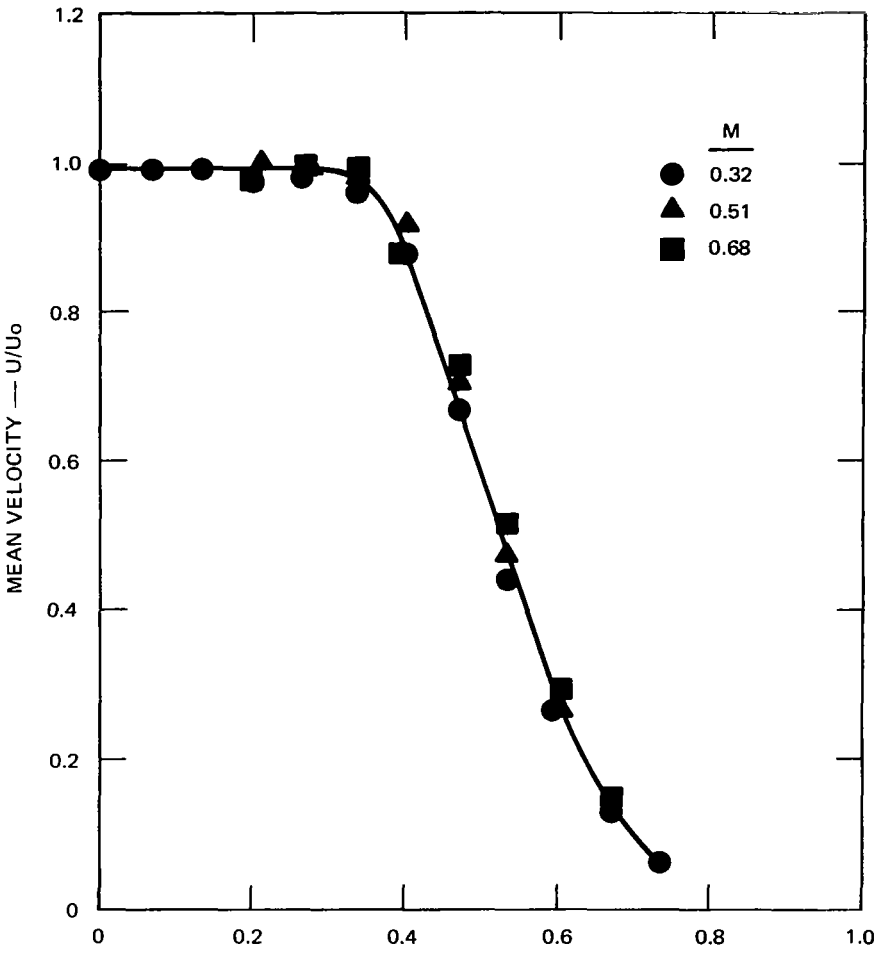

FIGURE 25 JET VELOCITY PROFILES AT VARIOUS MACH NUMBERS AT X/D = 2

levels of nozzle turbulence were investigated. The higher level of turbulence was induced by a 0.25-in. mesh X 0.05-in. diameter wire screen across and 0.5 in. inside the nozzle exit. The effects are shown in Figs. 26, 27, and 28. It is evident that at the higher turbulence level there is a broadening of the potential core, as can be seen in Fig. 26.

The effects of higher nozzle turbulence on the overall jet turbulence are noticed only at the higher Mach number as illustrated by Figs. 27 and 28, and most notably in the central core region (Y/D = 0).

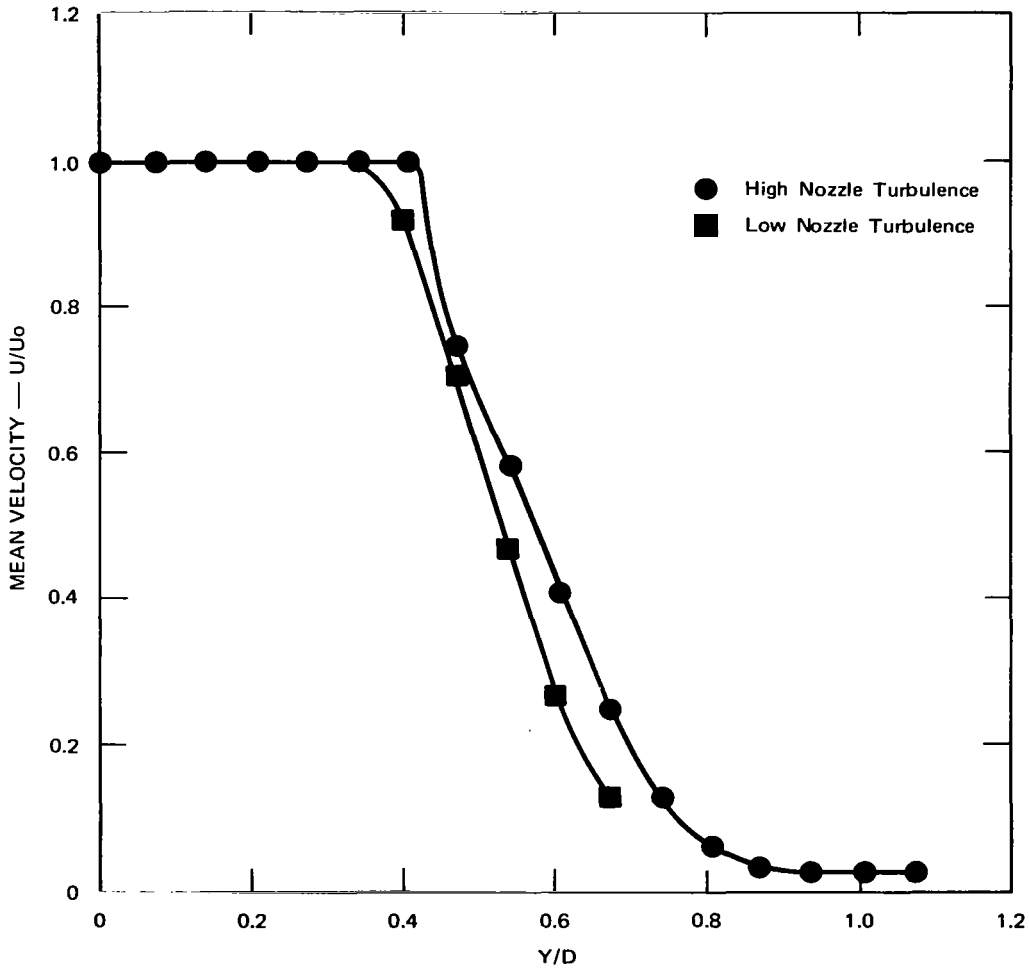

FIGURE 26 MEAN VELOCITY PROFILES COMPARING HIGH AND LOW TURBULENCE NOZZLES

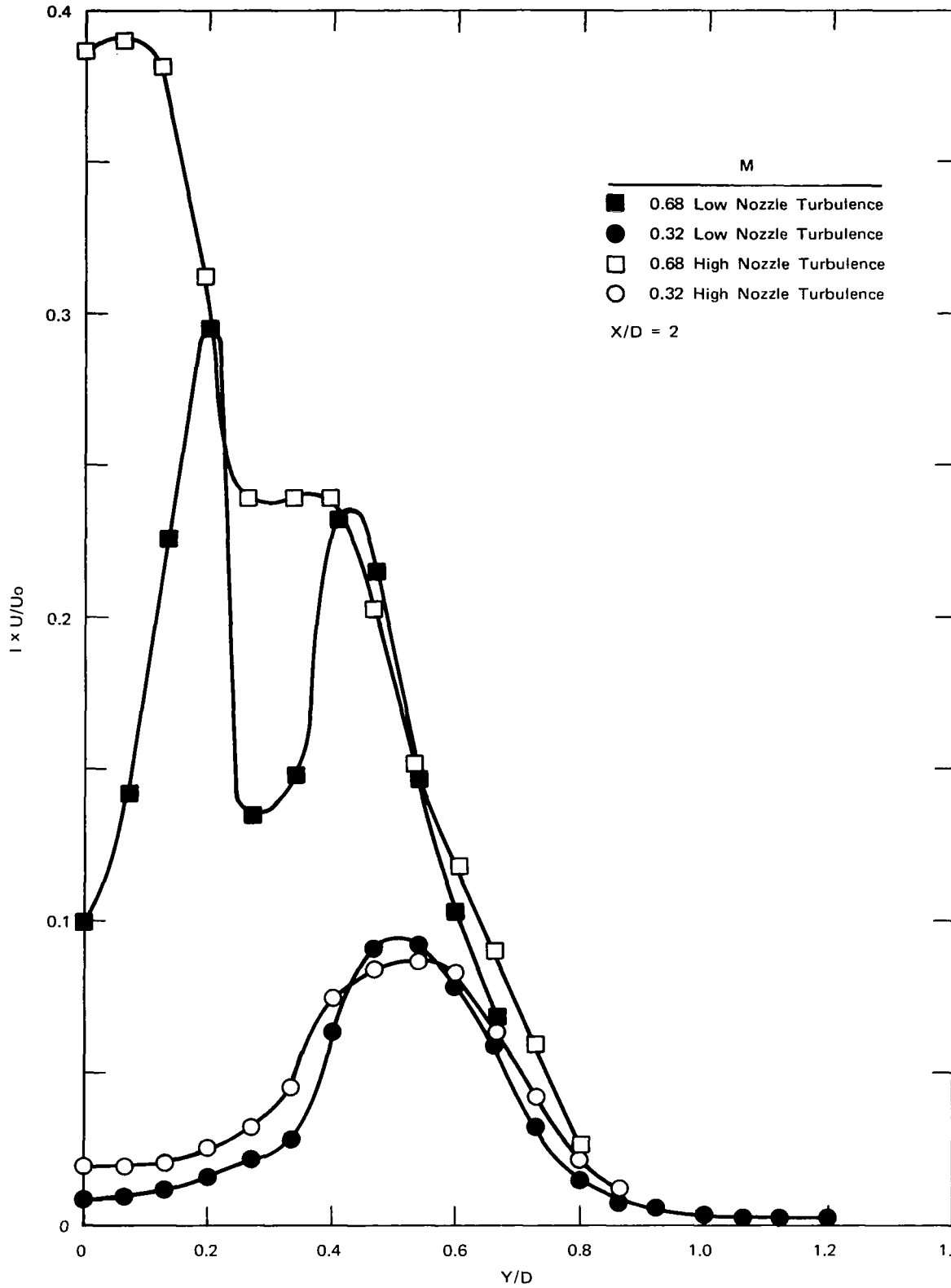

FIGURE 27 TURBULENT INTENSITY PROFILES COMPARING HIGH AND LOW NOZZLE TURBULENCE

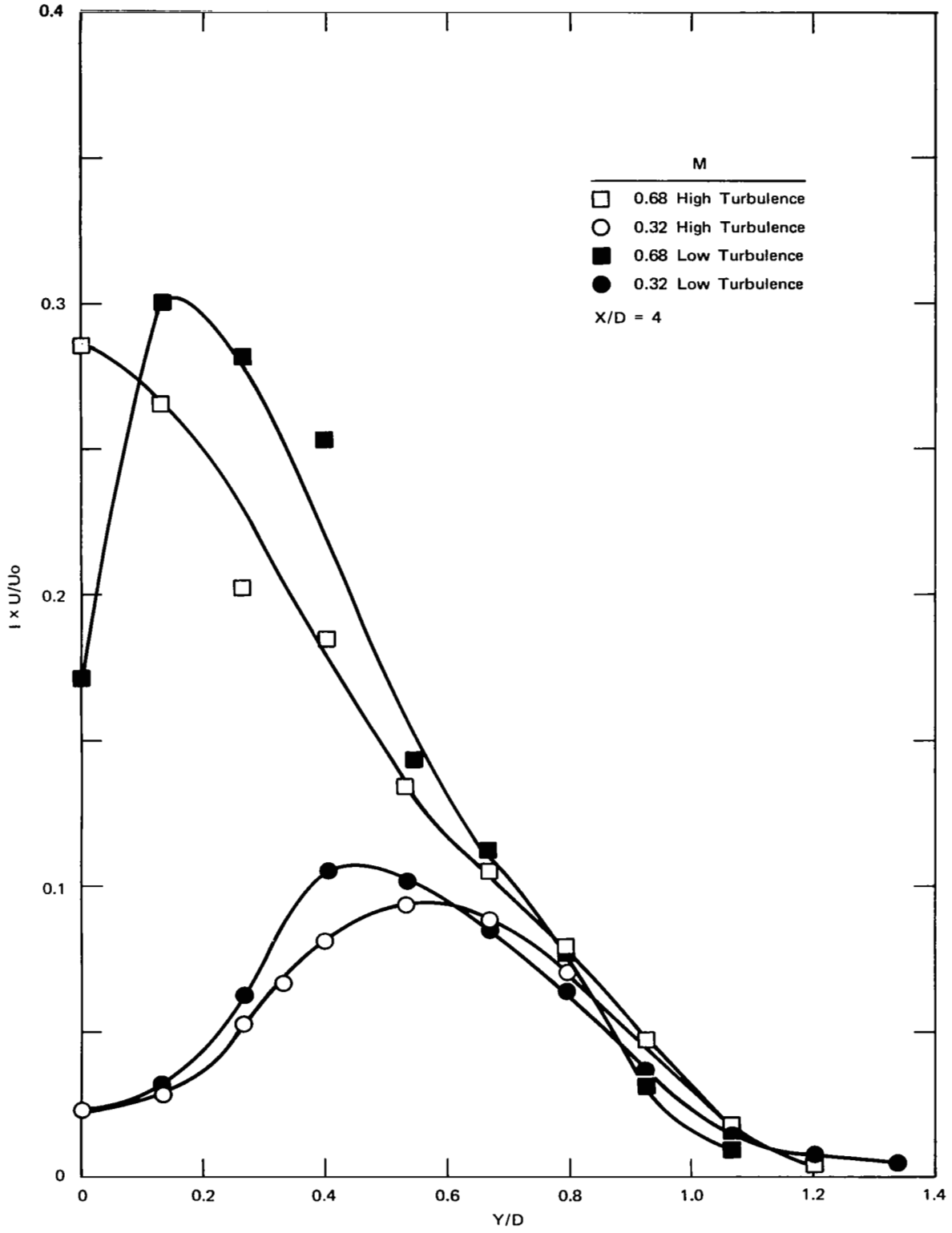

FIGURE 28 TURBULENT INTENSITY PROFILES COMPARING HIGH AND LOW NOZZLE TURBULENCE

IV DISCUSSION

The experiments presented in the previous section, once sources of anomalous turbulence signals were diagnosed and corrected, were primarily aimed at a thorough characterization of the overall jet structure, both with and without high levels of core turbulence. It is believed that great care must be exercised to characterize a jet in this manner before making measurements more directly related to noise production, since the results of such measurements are likely to be quite sensitive to any anomalous jet turbulence caused by upstream disturbances, resonances, etc. For example, from Fig. 17 it is quite clear that both the magnitude and radial distribution of the turbulent intensity can be altered drastically by the presence of such disturbances. Once the jet was well characterized and free from such anomalous effects, then measurements of the detailed structure of the noise-producing region of the jet turbulence (convection velocities, spectra, etc.) were carried out.

Little difference apparently exists between the mean velocity profiles of a jet with high and low core turbulence levels, as can be seen by a comparison of Figs. 19, 20, and 21 with Figs. 22, 23, and 24. The small difference between high and low core turbulence in the jet is shown in Fig. 26. At the higher Mach numbers, in particular, (where the core turbulence is relatively higher, see Fig. 26), the mean velocity profile is more squared at the boundary between the core region and the turbulent shear layer. Further investigations are required to determine the influence of core turbulence upon the detailed structure of the turbulent shear layer. However, it is reasonably certain that the intermittency at the core side of the shear layer is changed by higher

core turbulence levels, since there is a noticeable effect on the mean velocity profile at this location.

Measurements using two hot-wire probes, from which spectra, autocorrelations and cross correlations (used to compute convection velocities) were computed, were carried out for low core turbulence levels only. Now that the jet is free from anomalous behavior, and the A-D conversion and digital analysis computer programs have been written, however, further measurements under a wider variety of conditions are planned to assess more carefully the influence of core turbulence upon the noise-producing region of the turbulent jet.

General Results of Digital Analysis

The signals from each of the two hot wires used to make axial spatial correlations were analyzed in segments of 102.4-msec duration. The signals, recorded simultaneously on a tape recorder, were sampled digitally every 25 μsec, for a total of 4096 sample values per channel. After the data were read into the computer, the input signals were plotted using the CDC 280 microfilm plotter. An example of the input data is shown in Fig. 29. Channel A is the upstream wire of the pair. The vertical scale is an arbitrary binary scale chosen for convenience. A rough calibration was made, however, by analyzing a 1-kHz, 1-V rms signal, which indicates that each unit on the vertical corresponds to approximately 22 mV. A rigorous calibration was not carried out since absolute magnitudes do not enter the correlation measurements.

A digital analysis, described previously, was used to compute the autocorrelation function of each channel. The zero crossing of the autocorrelation was computed and printed on the top of the resulting plot. An example of such a plot is shown in Fig. 30. This curve represents the autocorrelation of the hot-wire signal in the fixed

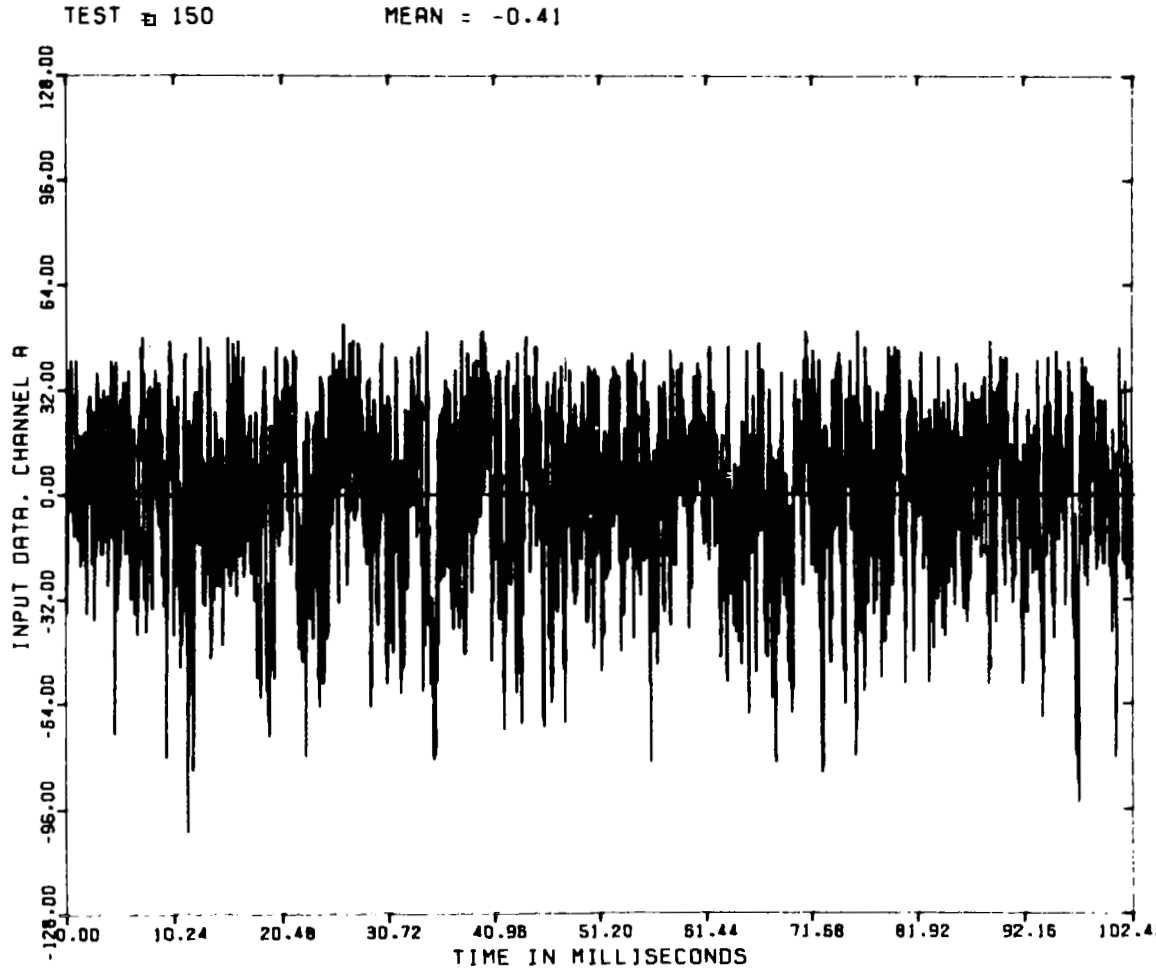

FIGURE 29 INPUT DATA: SIGNAL FROM UPSTREAM HOT WIRE

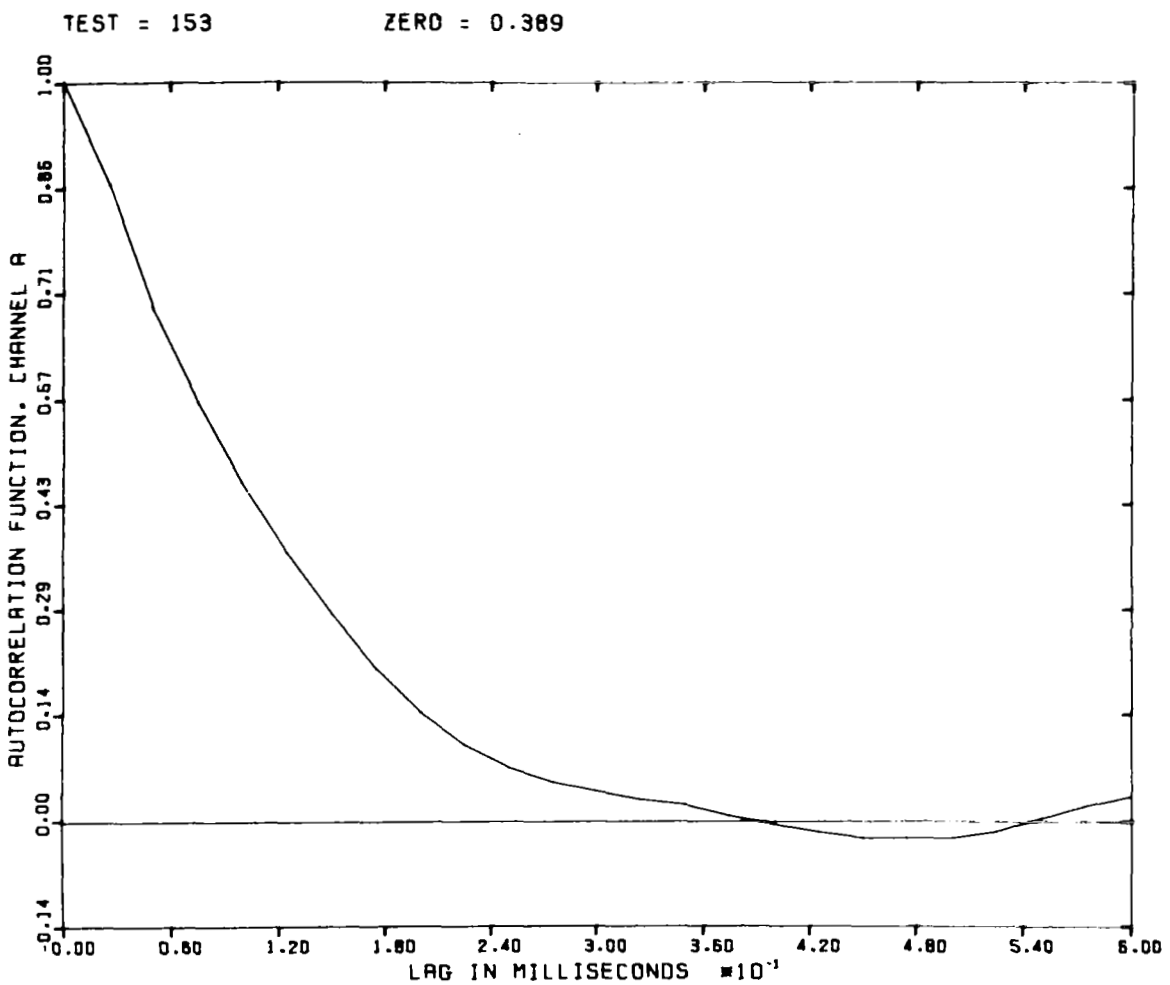

FIGURE 30 AUTOCORRELATION FUNCTION OF SIGNAL FROM UPSTREAM WIRE

(laboratory) frame of reference. The curve has a shape similar to that reported by other investigators.[18,27] Detailed analysis of these curves for jet turbulence has been reported by others[18,20,27] and will not be repeated here. It is worth noting, however, that the curve shapes and zero crossings for the two signals were in good agreement with each other, indicating no discrepancy between the upstream and downstream wires. It was interesting, however, that the autocorrelation of the signal from the downstream wire varied more smoothly for large wire spacing (after the final zero crossing). Since the shedding frequency for the hot wire is on the order of 100 kHz, this signal should die out very rapidly and is not likely to be the cause of this smoothing effect. Other than this, the two signals should be identical, so no reason for the smoothing of the downstream wire's autocorrelation at large time delay is readily apparent. This question will be examined further in later work.

A typical plot of power spectral density (PSD) is plotted in Fig. 31. The spectrum is scaled to unity power (i.e., unity area under the curve) and plotted relative to an octave frequency scale in which 11 octaves correspond to 20 kc, 10 octaves to 10 kc, etc. As will be shown, the spectral data are internally consistent and agree with observations of other investigators in similar jet flows.

The computed cross-correlation function R_{11}, between the signals from the two channels, was plotted for each test. The (three-point) interpolation of the maximum value of the cross-correlation and the corresponding time lag were listed at the top of the plot. The three-point interpolation was made by taking the maximum value and one point on each side of the maximum, and fitting these three points with a quadratic curve. The maximum value of the quadratic and the associated time lag are the values listed on the plot. Examples of computed cross-correlations are shown in Fig. 32 for two values of wire spacing, to

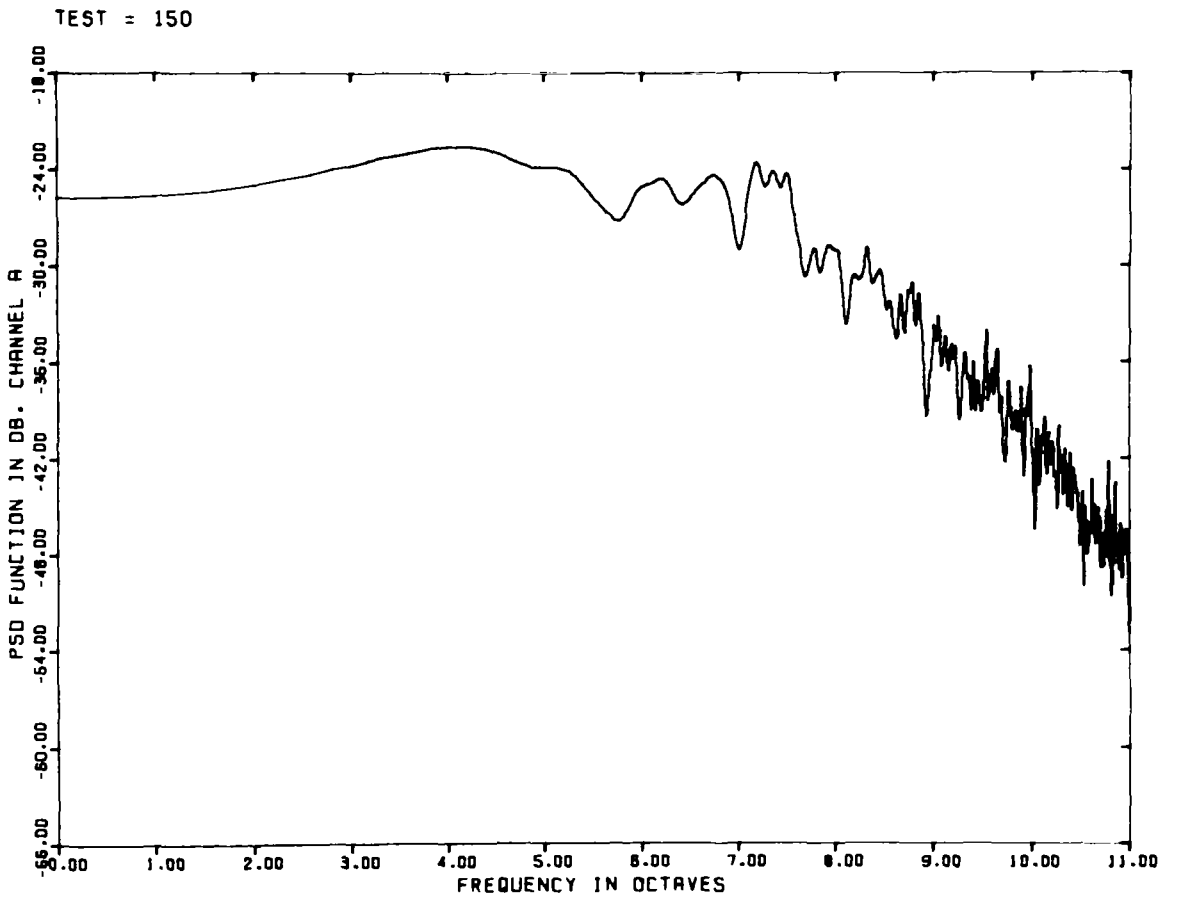

FIGURE 31 POWER SPECTRAL DENSITY OF SIGNAL FROM UPSTREAM WIRE

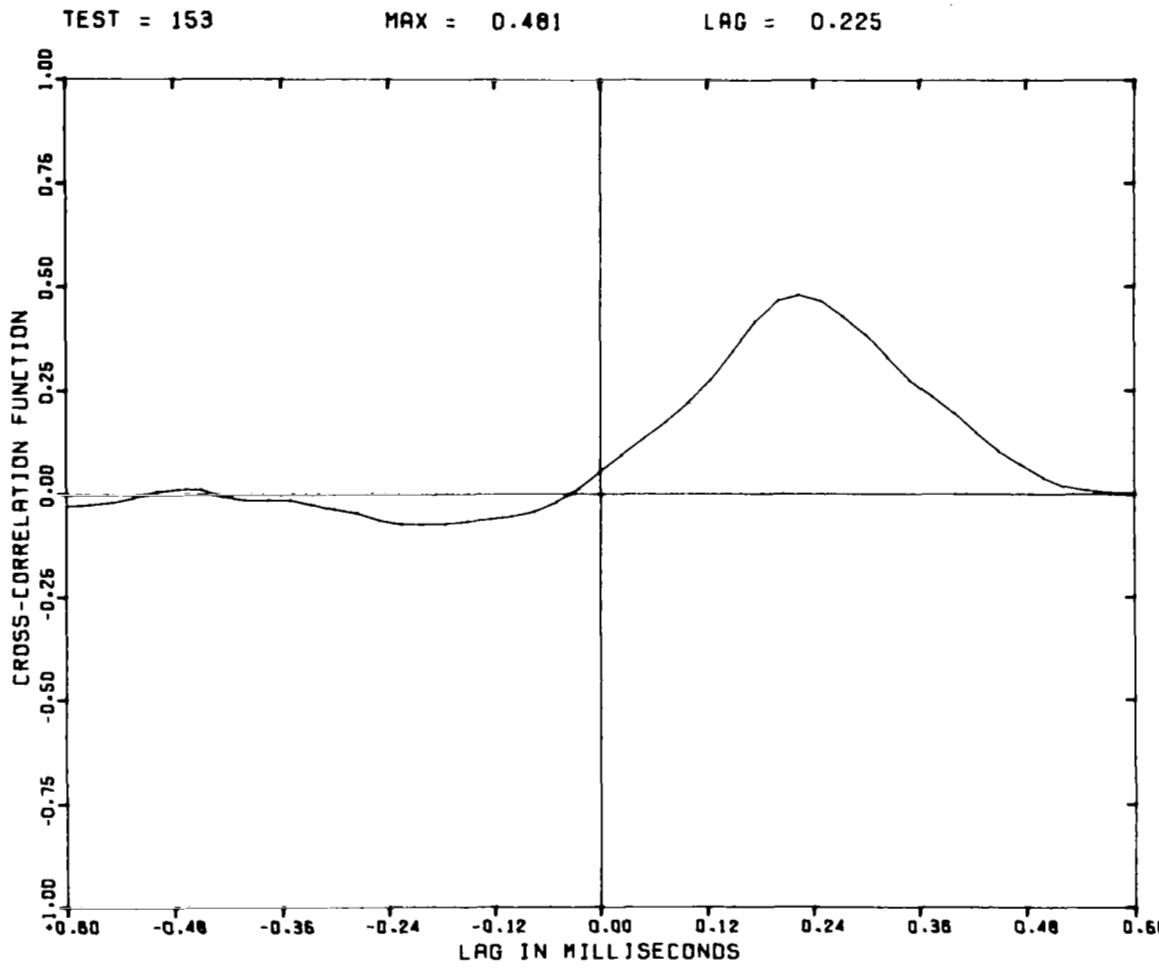

(a) WIRE SPACING = 1/8 in.

FIGURE 32 CROSS-CORRELATION FUNCTION R_{11} VERSUS TIME LAG

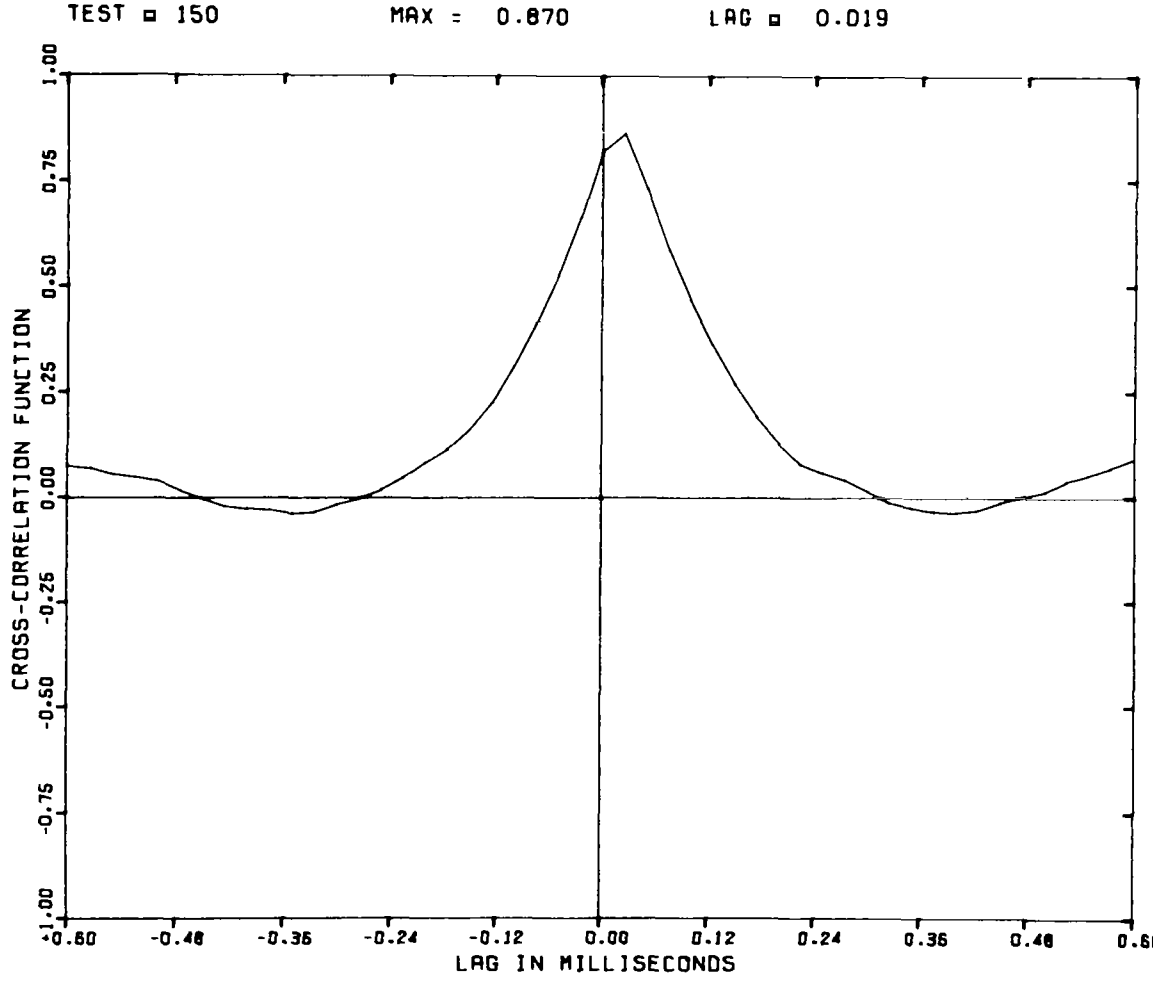

(b) WIRE SPACING = 1 in.

FIGURE 32 CROSS-CORRELATION FUNCTION R_{11} VERSUS TIME LAG (Concluded)

show how the peak values decrease and the associated time lags increase with increased wire spacing. In addition to curves like those shown in Fig. 32, the maximum value of the cross-correlation and five points on either side of the maximum, together with the corresponding time lags, were printed out along with the interpolated values for each test. These data were used to prepare plots of the cross-correlation from which convection velocities were computed for each set of measurements. These correlations will be discussed in more detail in a later section of the report. A listing of all tests for which axial velocity correlations were made is given in Table I. These tests were all analyzed using digital spectral analysis of the signals from both wires. The values of X/D correspond to the position of the upstream wire in each case and ΔX is the wire spacing. Both wires were kept at the same radial position in corresponding series of tests.

Turbulent Spectra of the Axial Velocity Component

Early measurements of mean velocity, turbulent intensity, and spatial correlations in the turbulent shear region adjacent to the potential core of a subsonic jet were made by Liepmann and Laufer.[28] These measurements were later extended by Laurence[18] to include turbulent velocity spectra. Actually, most of Laurence's measurements were made in the mixing region downstream of the potential core, but he does report several measurements in the shear layer adjacent to the core. More recently, Davies, Fisher, and Barratt[20] reported spectral measurements in the shear region of a 1-in. diameter jet. Their results indicate that the spectra at X/D = 1.5 do not change significantly with radial position and that at an axial position of X/D = 4.5 there is a systematic shift of energy to lower frequency with increasing radius. They reason from this that the convection velocity of the eddy pattern varies much less rapidly with radius than the mean velocity, a conclusion which they further substantiate

Table I

EXPERIMENTAL CONDITIONS FOR TESTS USED TO MEASURE CONVECTION VELOCITIES

Test	Wire Spacing ΔX (in.)	Axial Position Y/D	Mach Number M	Radial Position X/D
121	1/2	2	0.32	0.5
122	1			
123	2			
124	3			
125	1/16	2	0.51	0.5
126	1/8			
127	1/4			
128	1/2			
129	1			
130	2			
131	2	2	0.688	0.5
132	1			
133	1/2			
134	1/4			
135	1/8			
137	1/16	2	0.51	0.45
138	1/8			
139	1/4			
140	1/2			
141	1			
142	2			
143	1/16	2	0.51	0.6
144	1/8			
145	1/4			
146	1/2			
147	1			
148	2			
149	1/16	4	0.51	0.5
150	1/8			
151	1/4			
152	1/2			
153	1			
154	2			

by direct convection velocity measurements. (This phenomenon is discussed at length later in this report under the spatial correlation and convective velocity topics.) More recently still, Davies, Ko, and Bose[29] report more complete spectra measured at various radial positions for X/D = 3 in a 1-in. diameter jet. Their primary interest was to investigate the sharply peaked spectra, which are observed in the core region of the jet, and relate the Strouhal number of this peak to coherent pressure fluctuations observed across the jet in the core region.

Spectral measurements were made as a part of this research program to confirm the results obtained by the above investigators and to characterize the jet to ensure that no anomalous spectral behavior was present. The PSD of the axial velocity fluctuations is plotted as a function of dimensionless wave number in Fig. 33 to show the effect of radial position. As noted by Davies et al.,[20] there is a slight shift of energy to lower frequencies with increasing radial position. The PSD is normalized to unity power in each case, and the dimensionless wave number $\tilde{K}_1$ is defined as

$$\tilde{K}_1 = \frac{2\pi fD}{1100M} \frac{X}{D} \tag{18}$$

where f is the frequency, M is the jet Mach number (1100 ft/sec is taken as the reference sound speed), D is the jet diameter, and X the axial position. The axial position is chosen as the relevant length scale since the width of the turbulent shear region and hence the macroscopic, or integral length scale, is proportional to the axial distance from the jet exit. This proportionality was pointed out by Laurence[18] and in more detail by Davies et al.,[20] who measured the axial scale of the turbulence L_{x1}, and found that it can be expressed as

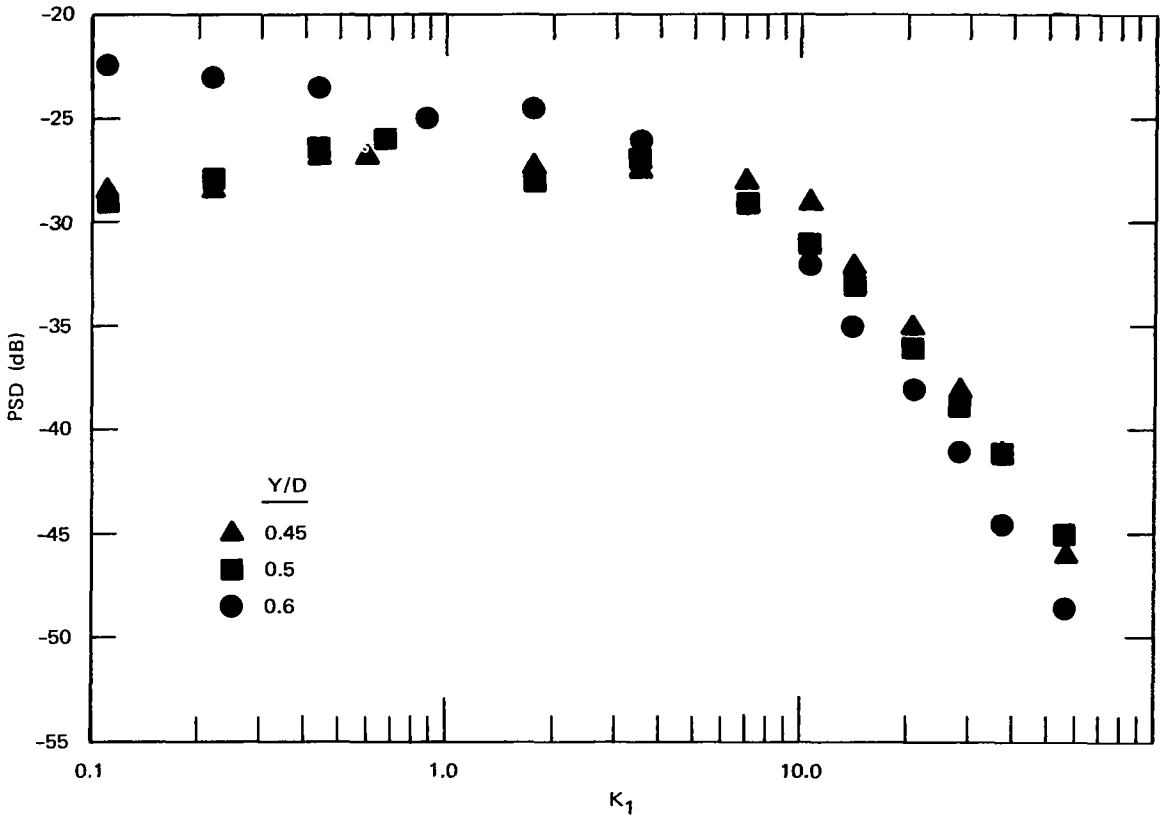

FIGURE 33 POWER SPECTRA VERSUS DIMENSIONLESS WAVE NUMBER AT DIFFERENT RADIAL POSITIONS

$$L_{x1} = 0.13\ X\ (D < X < 6D) \tag{19}$$

or

$$L_{x1} \simeq 0.52\Delta \tag{20}$$

where Δ is the width of the shear layer adjacent to the jet core.

Spectra for three Mach numbers and two axial distances are shown in Fig. 34. At the axial positions X/D = 2, the spectra for all three Mach numbers correspond closely at high frequencies. There is relatively more low frequency energy, however, in the spectra taken at the lower Mach numbers. In addition, the spectrum for X/D = 4 falls above all

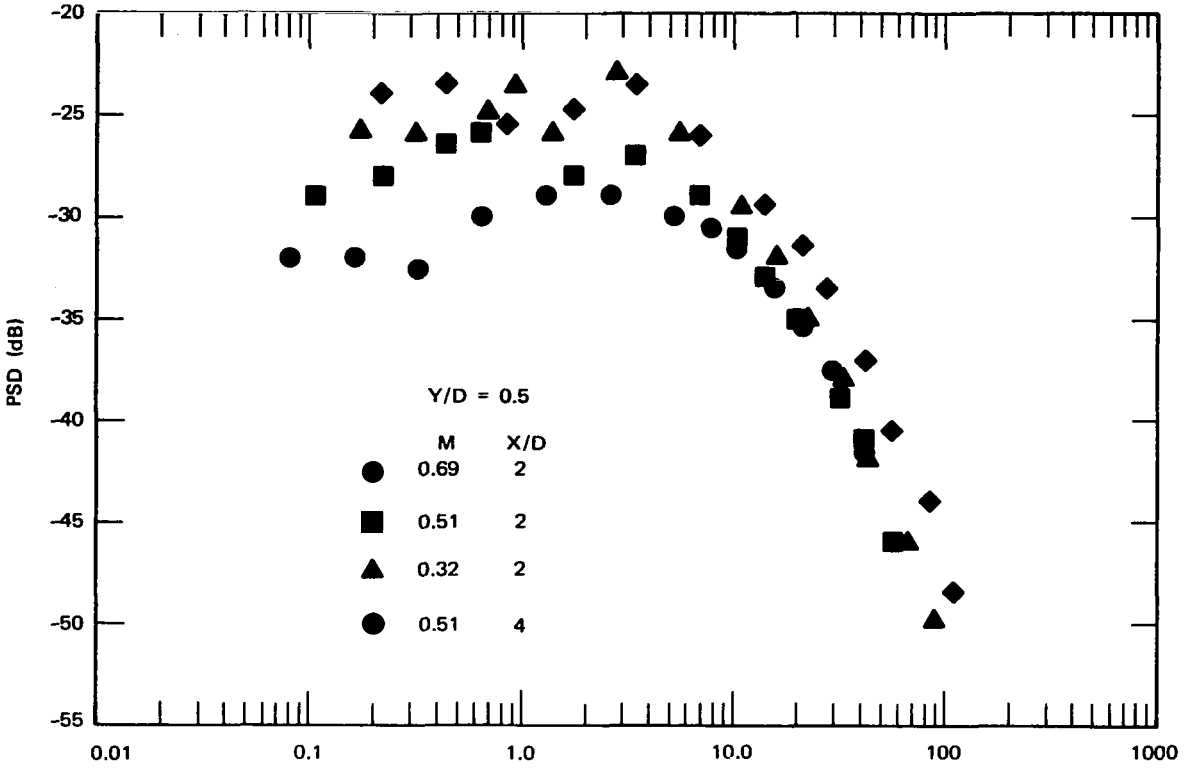

FIGURE 34 POWER SPECTRAL DENSITY VERSUS DIMENSIONLESS WAVE NUMBER AT DIFFERENT MACH NUMBERS

the spectra at X/D = 2, even at high frequencies. The lack of coincidence at high frequencies between the spectra taken at the two different axial positions is probably due to improper choice of the length scale used to nondimensionalize the wave number. A more suitable choice would be to use the integral length scale computed from the measured correlation. An alternate and perhaps better procedure is to nondimensionalize both the spectra and wave number in a way similar to that used by Wooldridge and Muzzy,[30] who analyzed the turbulent velocity spectra in a boundary layer flow. In subsequent work, it is planned to nondimensionalize properly the spectra and wave number and compare the high frequency spectra with the theoretical spectrum derived by Pao[31] for homogeneous turbulence. For the present, however, the use

of jet velocity and axial distance to nondimensionalize the wave number and the normalization of the spectra to unity are sufficient to characterize the jet and make comparisons with data taken by other investigators.

The recent PSD measurements by Davies et al.[29] in a 1-in. jet are compared with present measurements in Fig. 35. Because different reference levels were used in the two measurements, the data were plotted so that the reference dB level of Davies' work was changed to correspond to that of the present work. Thus, the PSD was first plotted for each experiment on separate graphs, and then the two were slid vertically for best fit. Clearly, the shape of the two spectra correspond very closely, indicating good agreement between the two sets of data. (Note that the Mach numbers and axial positions do not differ greatly in the

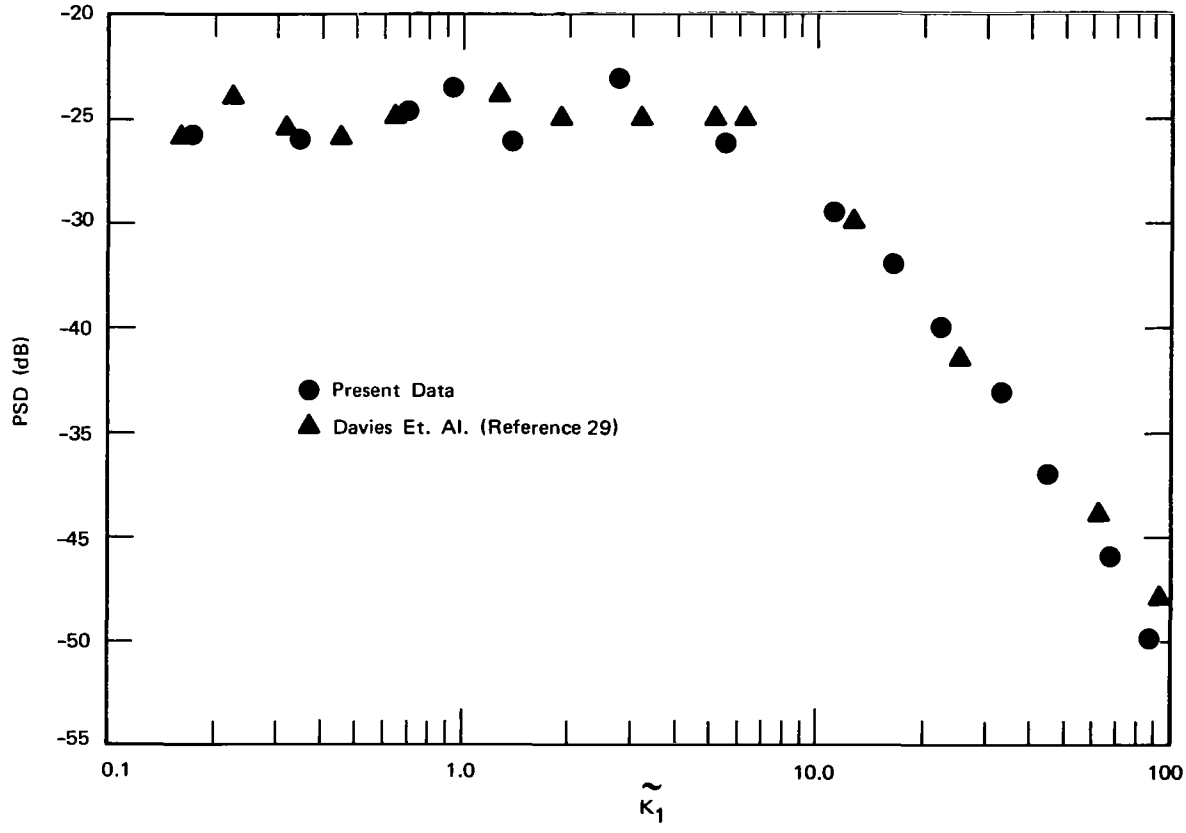

FIGURE 35 POWER SPECTRAL DENSITY COMPARISONS FROM DIFFERENT INVESTIGATORS

two cases and the radial positions are equivalent, so that the differences due to radial and axial position, as indicated in Figs. 33 and 34, are not apparent.) For further comparison and as a check on the digital data analysis, the spectrum was measured from the hot-wire signal using a wave analyzer. The resulting analog spectrum was normalized in the same way as Davies' data to a reference dB level adjusted for best fit.

Convection Velocity Measurements

Measurements of convection velocities in turbulent jets have been reported by several investigators. Davies et al.[20,29] reported convection velocity measurements in which the axial convection velocity profile, scanned radially across the jet, is compared with the mean axial velocity profile. They found that, for the radial position $Y < D/2$, the convection velocity U_c is less than the mean axial velocity U and, for $Y > D/2$, U_c is greater than U. Davies' curve is shown in Fig. 36. Bradshaw, Ferriss, and Johnson[27] reported similar results, as did Wills.[32] That the axial convection velocity varies more slowly across the shear layer adjacent to the jet core than the mean velocity is thus well established experimentally. Davies, Fisher, and Barratt,[20] Davies,[33] Fisher, and Davies,[34] and Richards[35] explain this phenomenon physically in terms of the probability density of the turbulent velocity fluctuations. Basically, the large scale fluctuations to one side of the centerline of the shear layer contain large components of the characteristic free stream velocity just outside the shear layer. That is, on the jet core side ($Y < D/2$) of the center of the shear layer, the large scale velocity fluctuations carry significant energy characteristic of the core velocity. Fisher and Davies[34] show how these eddies influence the cross-correlation measurements in such a way as to cause the observed differences between the mean velocity and convection velocity across the mixing region.

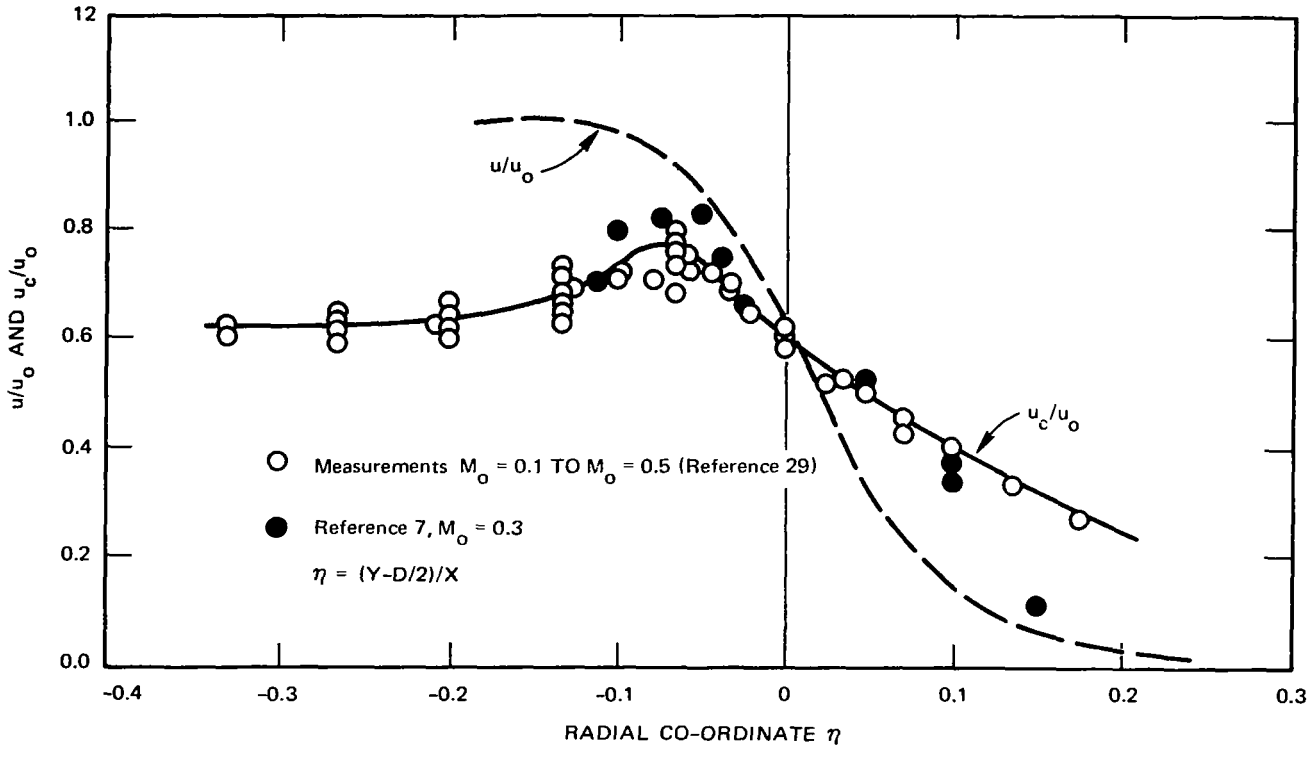

FIGURE 36 RADIAL DISTRIBUTION OF AXIAL CONVECTION VELOCITY

In addition to the overall convection velocity measurements, Fisher and Davies[34] measured convection velocity for several frequency bands. Their measurements were made to determine whether or not various wave-number (frequency) components are convected downstream at the same velocity. Their data were taken only for the radial position Y/D ≈ 1/2 and indicated that the convection velocity increased slightly with increasing center band frequency of the filtered signals. It is still not clear, however, how the convection velocities of the various frequency components are convected at different radial positions in the jet. Figure 36 represents the overall convection velocity measurements and, as such, does not give frequency (eddy size) resolution.

It is of interest, and explored in a subsequent section of this report, how a plot similar to Fig. 36 would look, plotted for various frequency components. First, as a check on the consistency of the data, convection velocities were measured using the unfiltered cross-correlation measurements. Then for three radial positions at X/D = 2, cross-correlations for data numerically filtered in three narrow bands were used to measure the frequency dependence of the convection velocity.

Unfiltered Convection Velocity Measurements

Plots of the cross-correlation of the unfiltered axial velocity fluctuation as a function of dimensionless time delay for several constant hot-wire spacings were used to compute the overall eddy convection velocity. Examples of these plots are shown in Figs. 37, 38, and 39 for Mach numbers of 0.32, 0.51, and 0.688, respectively, at X/D = 2. The dimensionless time delay $\tilde{t}$ is defined as

$$\tilde{t} = \frac{1100MD}{X/D} t \qquad (21)$$

where t is the dimensional time delay. This has the effect of giving a rough correspondence between correlations made under differing conditions. Strictly speaking, the characteristic time [= X/(1100M)] in Eq. (21) should be referred to the local time scale of the turbulent fluctuations. However, since this scale was not computed in these experiments, Eq. (21) was used instead. The resulting convection velocities are the same in either case.

To obtain the delay time associated with each value of wire spacing, the envelope tangent to each correlation curve and passing through $R_{11} = 1$ at zero time delay was drawn. The point of tangency of this envelope then determines the time delay to be used with each wire spacing to compute convection velocity. For example, in Fig. 37 the

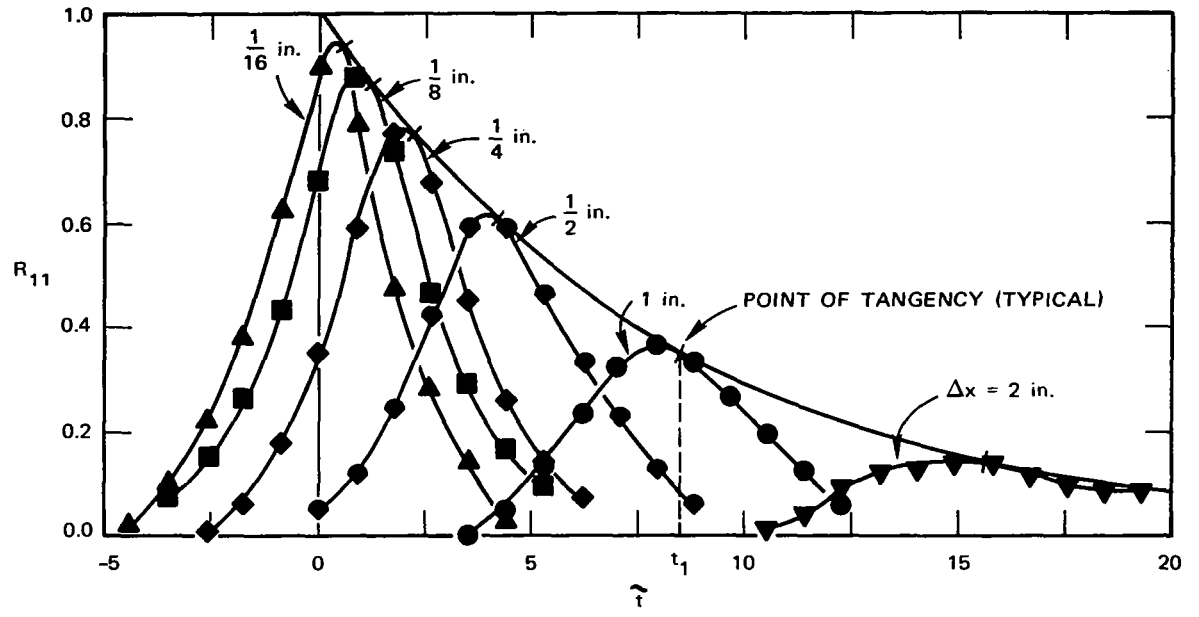

FIGURE 37 CROSS-CORRELATION OF AXIAL VELOCITY FLUCTUATION VERSUS TIME DELAY FOR VARIOUS HOT-WIRE SPACING.

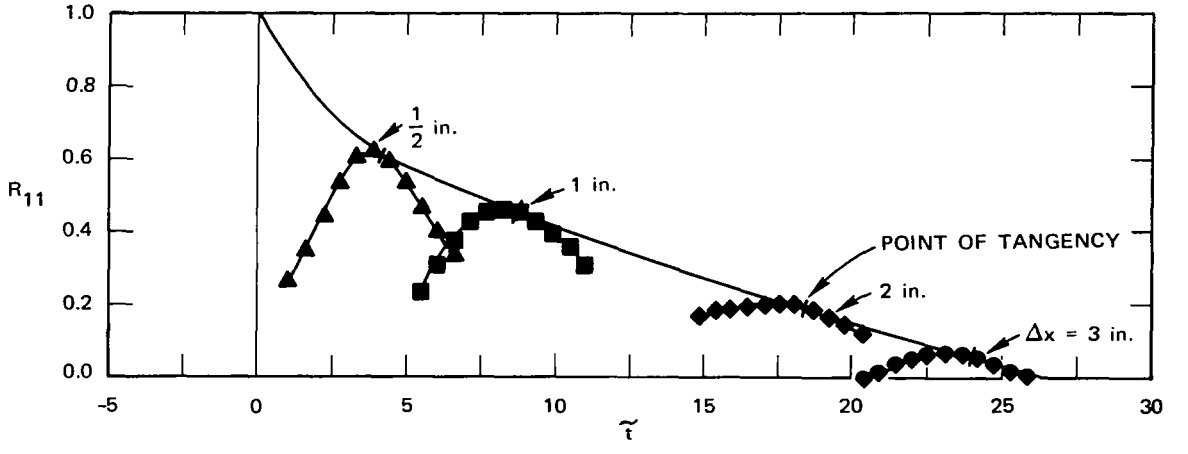

FIGURE 38 CROSS-CORRELATION OF AXIAL VELOCITY FLUCTUATION AS A FUNCTION OF HOT-WIRE SPACING

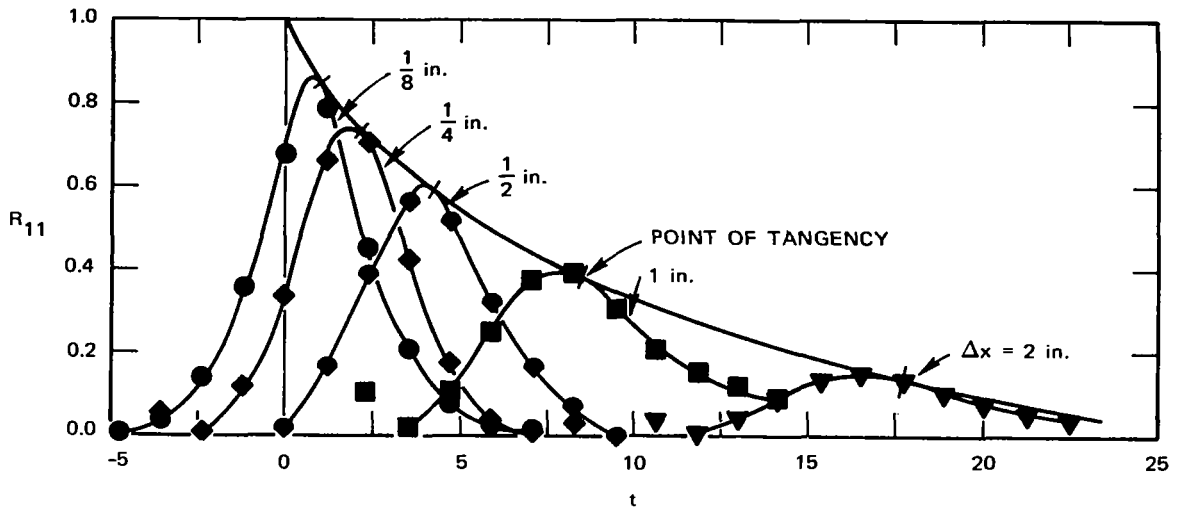

FIGURE 39 CROSS-CORRELATION OF AXIAL VELOCITY FLUCTUATIONS AS A FUNCTION OF HOT-WIRE SPACING

time delay $\tilde{t}_1$ associated with the wire spacing of 1 inch is shown. (Note that the time delay determined in this way does not correspond to the time delay for maximum cross-correlation.) The convection velocity, then is given by

$$U_c = \frac{\Delta X}{\tilde{t}_1}\left(\frac{1100MD}{X/D}\right) \quad . \tag{22}$$

The convection velocity, using Eq. (22), is then computed for each wire spacing and associated time delay, and averaged to determine the mean convection velocity. In most cases, the convection velocities for all wire spacings in a given test corresponded very closely. However, in the high-frequency band-pass correlations described later, the correlation rapidly dies out as wire spacing is increased. More uncertainty results since only the correlation for close wire spacings can be used; hence errors in reading time delay produce relatively greater scatter in the data. However, even for the high frequency correlations, at least three tangency points were readable so that the resulting average convection velocity was considered to be of acceptable accuracy.

Determination of the time delay associated with each wire spacing at the tangency point with the envelope of the cross-correlation curves gives the convection velocity of the frame of reference in which the turbulence decays least rapidly. The envelope curve, then, is the auto-correlation that would be measured in a frame of reference moving at the convection speed.

The overall convection velocities, measured in this way, are compared in Fig. 40 with the mean velocity and with the data taken by other workers, which was shown in the paper by Davies, Ko, and Bose.[29] The present results agree to within the scatter presented in Davies' work. Apparently the peak shown in the previous work for $0.4 < Y/D < 0.5$ may not be present in the current measurements. This possibility will be checked with more measurements in future work.

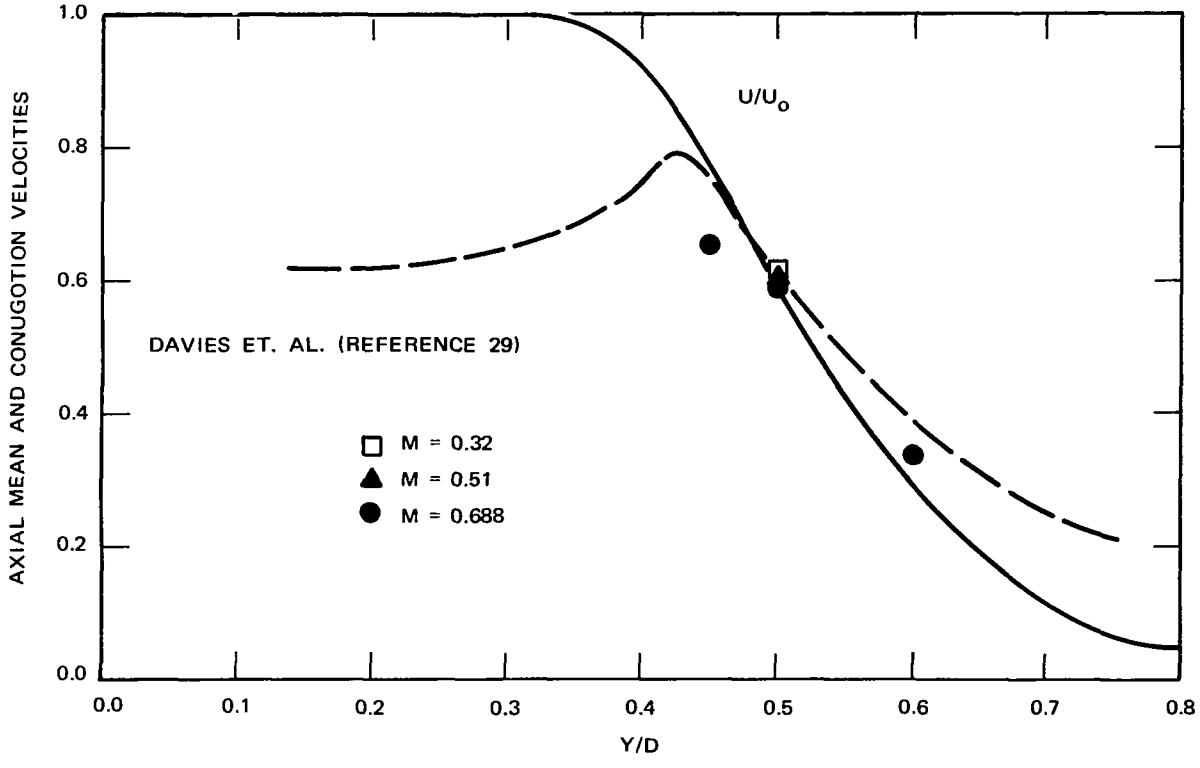

FIGURE 40 CONVECTION VELOCITY OF COMPLETE SIGNAL COMPARED WITH DATA GIVEN BY OTHER INVESTIGATORS

Band-Pass Measurements - Convection Velocity as a Function of Frequency

To measure the convection velocities of various frequency components of the axial velocity fluctuations, the signals were numerically filtered using three narrow-band filtering functions. After computing the PSD of each channel of a given test, the spectrum was filtered using each of the three following digital filtering functions,

Low Band Pass -

$$= \cos^2 [\pi(j - 100)/80] \quad , \qquad 60 \leq j \leq 140$$
$$= 0 \qquad\qquad\qquad\qquad\quad j < 60, \; j > 140$$

Medium Band Pass -

$$= \cos^2 [\pi(j - 400)/320] \quad , \qquad 240 \leq j \leq 560$$
$$= 0 \qquad\qquad\qquad\qquad\quad j < 240, \; j > 560$$

High Band Pass -

$$= \cos^2 [\pi(j - 1000)/800] \quad , \qquad 600 \leq j \leq 1400$$
$$= 0 \qquad\qquad\qquad\qquad\quad j < 60, \; j > 1400$$

where the frequency associated with each value of j is

$$f_j = \frac{10j}{2048} \text{ kHz} \quad .$$

The resulting spectra after the numerical filtering are shown (superimposed) on a PSD vs. frequency plot in Fig. 41. The center frequency of each band is 0.875, 3.5, and 8.5 kHz, respectively. The autocorrelation function of the signal in each band is shown in Fig. 42. As expected, the autocorrelation of the narrow-band signals resembles a damped cosine curve. The first zero-crossing, which is proportional to the macroscopic or integral time scale of the signal in that frequency

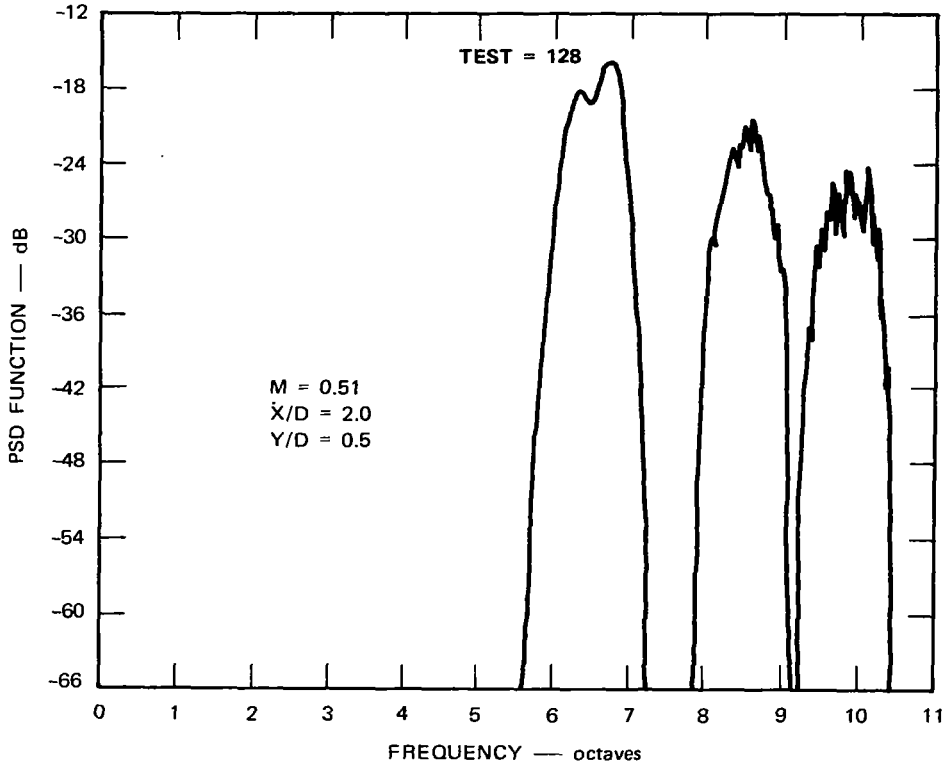

FIGURE 41 SPECTRA IN FREQUENCY BANDS CHOSEN FOR MEASUREMENTS OF AXIAL CONVENCTION VELOCITY AS A FUNCTION OF EDDY SIZE

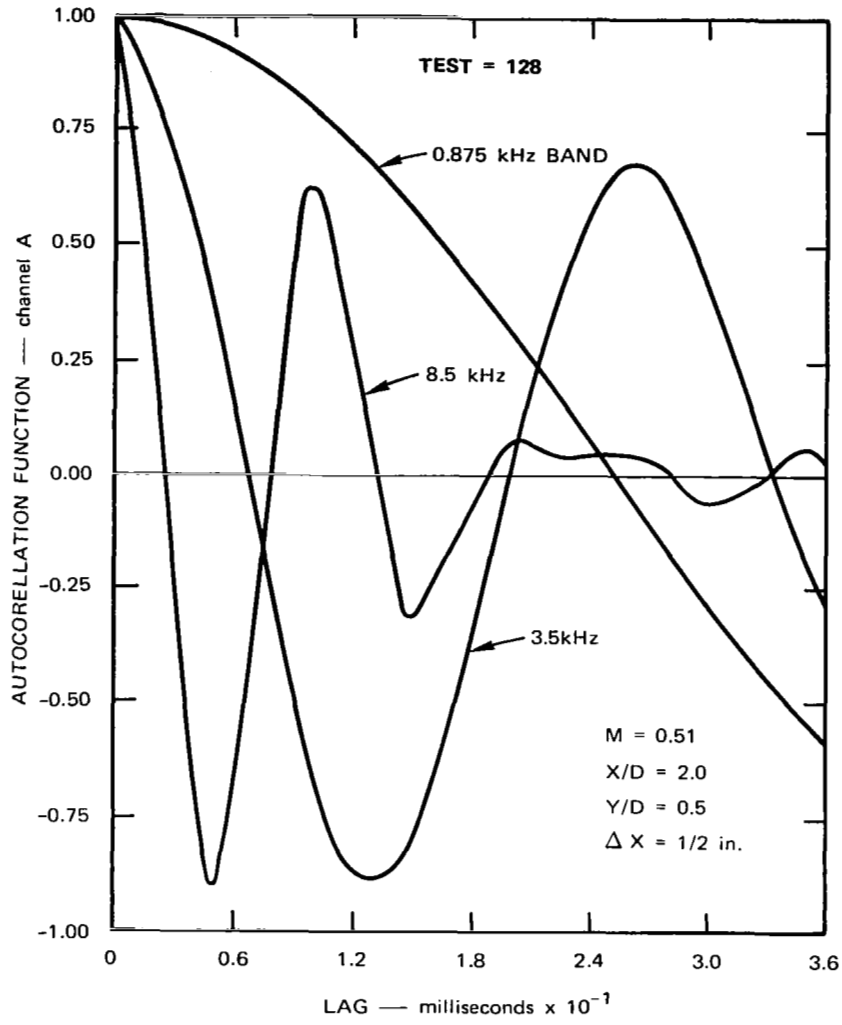

FIGURE 42 AUTOCORRELATION FUNCTIONS OF AXIAL TURBULENT VELOCITY FLUCTUATIONS FOR NARROW FREQUENCY BANDS

band, decreases with increasing frequency. Similar results are shown by Laurence.[18] The choice of band width for these computations was a matter of convenience. As demonstrated by Laurence,[18] the band width does not affect the portion of the autocorrelation of interest--that part between zero time delay and the first zero crossing. Rather, a narrower band width just causes the autocorrelation to go more negative (i.e., reduces the apparent damping).

The cross-correlations, calculated from the filtered data, were used to prepare plots from which convection velocities were computed. The results give the convection velocity as a function of frequency (eddy size). Data for three radial positions, at the axial position X/D = 2, and for a Mach number of 0.51, are plotted in Fig. 43. The

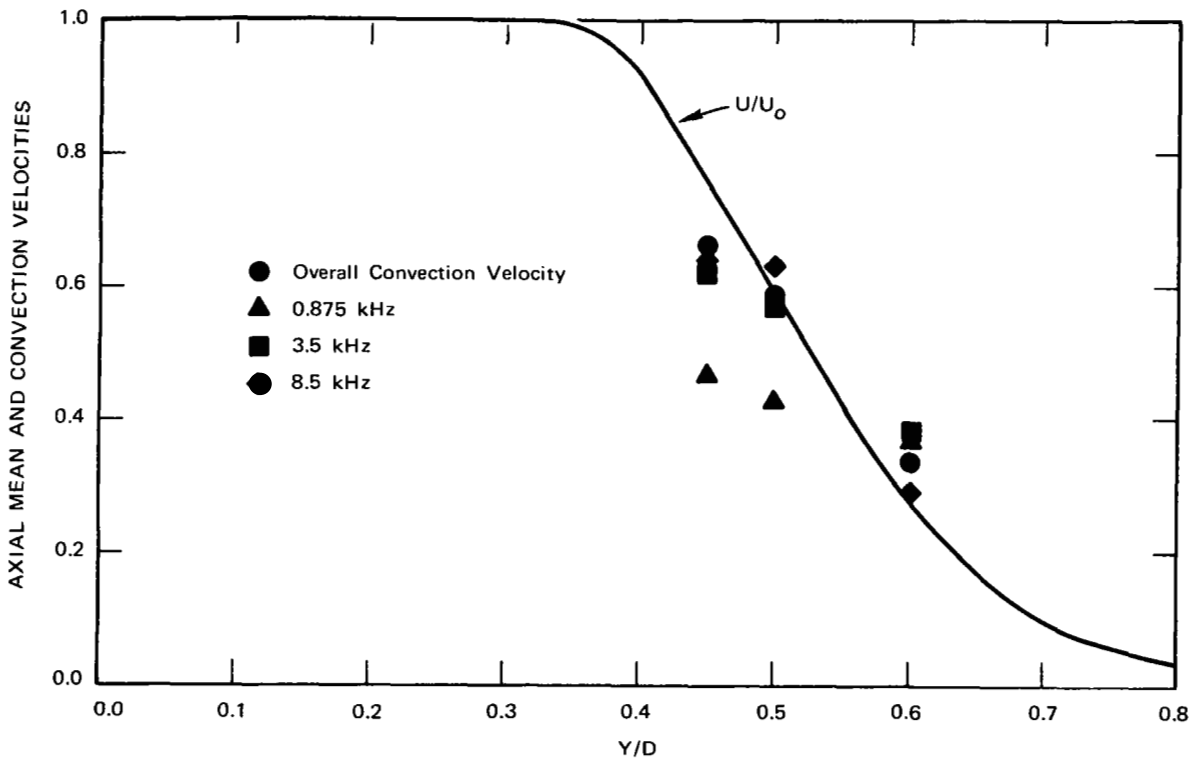

FIGURE 43 RADIAL DISTRIBUTION OF CONVECTION VELOCITY SHOWING VARIATION WITH FREQUENCY

overall convection velocity for the unfiltered signal is included for comparison. The lower frequency eddies (0.875 kHz center frequency) are convected at a significantly slower speed on the inner side of the center of the shear layer ($Y/D < 0.5$). The higher frequencies are convected at more nearly the mean velocity and are, in fact, convected at speeds very close to the overall convection velocity. For the radial position, $Y/D \approx 0.6$, there is not much difference between the convection velocities of various frequency components. In addition, the convection velocity of the low frequency components does not change much across the region of highest shear at the center of the shear layer. However, data are required at lower frequencies and for a wider range of radial positions to establish clearly the trends observed here. Additional measurements of this type are planned for the next stage of the current investigation. It is expected that the low frequency components of the turbulence will be convected at more nearly a constant velocity (around $0.5\ U_o$) and that the higher frequency components will be convected at speeds closer to the local mean velocity.

It is believed that the coherent pressure disturbances observed by Davies, Ko, and Bose[29] in the core region of the jet, which have a convection velocity of about $0.6\ U_o$, are caused by the ragged edge (intermittence) of the turbulent shear region around the potential core. The intermittence is associated with the larger turbulent eddies. Hence, since the scale of the larger eddies is on the order of the thickness of the shear layer, it is expected first, that the convection speed of these eddies will not vary significantly across the shear layer and second, that the convection speed should fall between, perhaps, 0.4 to $0.6\ U_o$. The results given in Fig. 43 show the correct trends; however, further work is required to confirm these relationships.

V CONCLUDING REMARKS

The gradual accumulation through the years of both far-field jet noise measurements and internal jet turbulence structure measurements, of which the current work is an extension, is leading toward an understanding of the physical mechanism by which jet noise is produced. Noise measurements in the far-field show that, from a noise-generation point of view, the jet is analogous to a train of convected quadrupoles traveling at a speed that is roughly 0.6 of the core velocity; i.e., at a velocity very close to that observed at the middle of the shear layer along a line directly downstream from the lip of the jet.

Cross-correlation measurements in frequency bands, which were begun under the current program, show that the largest-scale turbulence, having a scale of order of the local mixing region thickness, also tends to be convected at the mid-shear-layer velocity. The hypothesis follows directly that the preponderance of the observed sound is generated in the undisturbed core by interaction with the largest eddies, which may be considered circumferentially symmetric ("doughnut-shaped") and shed from the lip of the jet outlet.

Future studies in our laboratory will be devoted to a clarification of the above hypothesis by determining whether or not the large-scale turbulence is in fact symmetric. The next step, of course, is to inquire whether the symmetry could be destroyed by some means and to determine what effect such destruction would have on the generated noise.

REFERENCES

1. U.S. Congress, House of Representatives, Document No. 339, 89th Congress, 2nd Session, 1966, p. 2.

2. Great Britain, Board of Trade, "Aircraft Noise--Report of an International Conference on the Reduction of Noise and Disturbance Caused by Civil Aircraft," Her Majesty's Stationery Office, London, 1967.

3. Richards, E. J., "Aircraft Noise--Mitigating the Nuisance," J. Astro. Aero. 5, 34-43 (January 1967).

4. Golovin, N. E., "Alleviation of Aircraft Noise," J. Astro. Aero. 5, 71-75 (January 1967).

5. Bishop, D. E., "Judgments of Relative and Absolute Acceptibility of Aircraft Noise," Acoust. Soc. Am., 40, (1966).

6. Levin, S. M., "Aircraft Noise--Can it be Cut?" Space/Aeronautics 45, 65-75 (August 1966).

7. Lighthill, M. J., "Jet Noise," AIAA J. 1, 1507-1517 (July 1963).

8. Committee on the Problem of Noise, "Noise," Final Report, Her Majesty's Stationery Office, London, July 1963, Reprinted 1966, pp. 618-680.

9. Palo Alto Times, "Supersonic Jet Project Under Overall Review," Palo Alto, California, May 2, 1968, p. 7.

10. Harris, C. M., Handbook of Noise Control, McGraw-Hill Book Company, New York, 1957.

11. Lighthill, M. J. "On Sound Generated Aerodynamically. I. General Theory," Proc. Roy. Soc. (London) A211, 564-587 (1952).

12. Lighthill, M. J., "On Sound Generated Aerodynamically. I. Turbulence as a Source of Sound," Proc. Roy. Soc. (London) A222, 1-32 (1954).

13. Lighthill, M. J., "The Bakerian Lecture 1961, Sound Generated Aerodynamically," Proc. Roy. Soc. (London), A267, 147-182, (1962).

14. Powell, A., "Concerning the Noise of Turbulent Jets," J. Acoust. Soc. Am. 32 (12), 1609 (1960).

15. Powell, A., "Theory of Vortex Sound," J. Acoust. Soc. Am. 36(1), 177-195 (1964).

16. Williams, J.E.F., "On the Development of Mach Waves Radiated by Small Disturbances," J. Fluid Mech. 22, 49-55 (1965).

17. Williams, J.E.F., "Sound Radiation from Turbulent Boundary Layers Formed on Compliant Surfaces," J. Fluid Mech. 22, 347-358 (1965).

18. Laurence, J. C., "Intensity, Scale, and Spectra of Turbulence in the Mixing Region of a Free Subsonic Jet," NACA Report 1292, 1956.

19. Laurence, J. C., and Beninghoff, J. M., "Turbulence Measurements in Multiple Interfering Air Jets," NACA TN 4029, 1957.

20. Davies, P.O.A.L., Fisher, M. J., and Barratt, M. J., "The Characteristics of the Turbulence in the Mixing Region of a Round Jet," J. Fluid Mech. 22, 337-367 (1963).

21. Fitzpatrick, H. M., and Lee, R., "Measurements of Noise Radiated by Subsonic Air Jets," David Taylor Model Basin Report 835, 1952.

22. Lassiter, L. W., "Turbulence in Small Air Jets at Exit Velocities Up to 705 Feet per Second," J. Appl. Mech. 24, 349-354 (1957).

23. Lee, R., "Free-Field Measurements of Sound Radiated by Subsonic Air Jets," David Taylor Model Basin Report 868, 1953.

24. Lassiter, L. W., and Hubbard, H. H., "Experimental Studies of Noise from Subsonic Jets in Still Air," NACA TN 2757, 1952.

25. Hinze, J. O., Turbulence, McGraw-Hill Book Company, New York, 1959, Chapters 2 and 6.

26. Singleton, R. C., and Poulter, T. C., "Spectral Analysis of the Call of the Male Killer Whale," IEEE Trans. on Audio and Electroacoustics, AU-15, 104-113 (June 1967).

27. Bradshaw, P., Ferriss, D. H., and Johnson, R. F., "Turbulence in the Noise-Producing Region of a Circular Jet," J. Fluid Mech. 19, 591-624 (1964).

28. Liepmann, H. W., and Laufer, J., "Investigation of Free Turbulent Mixing," NACA-TN 1257, (1947).

29. Davies, P.O.A.L., Ko, N.W.M., and Bose, B., "The Local Pressure Field of Turbulent Jets," ARC-CP 989, (1968).

30. Wooldridge, C. E., and Muzzy, R. J., "Boundary-Layer Turbulence Measurements with Mass Addition and Combustion," AIAA J., 4, 2009-2016 (November 1966).

31. Pao, Y. H., "Structure of Turbulent Velocity and Scalar Fields at Large Wavenumbers," Phys. Fluids 8, 1063-1075 (June 1965).

32. Wills, J.A.B., "On Convection Velocities in Turbulent Shear Flows," J. Fluid Mech., 20, 417-432 (1964).

33. Davies, P.O.A.L., "Turbulence Structure in Free Shear Layers," AIAA J., 4, 1971-1978 (November 1966).

34. Fisher, M. J., and Davies, P.O.A.L., "Correlation Measurements in a Non-frozen Pattern of Turbulence," J. Fluid Mech., 18, 97-116 (1964).

35. Richards, E. J., "Recent Developments in Jet Noise Research," Proc. 3rd Int. Congr. on Acoustics. (1954).

NASA-Langley, 1971 — 12 CR-1836